

The ReSWARM Microgravity Flight Experiments: Planning, Control, and Model Estimation for On-Orbit Close Proximity Operations

Bryce Doerr*

Department of Aeronautics and Astronautics
Massachusetts Institute of Technology
77 Massachusetts Avenue, Cambridge, MA 02139
bdoerr@mit.edu

Keenan Albee*

Department of Aeronautics and Astronautics
Massachusetts Institute of Technology
77 Massachusetts Avenue, Cambridge, MA 02139
albee@mit.edu

Monica Ekal*

Institute for Systems and Robotics
Instituto Superior Técnico
Avenida Rovisco Pais 1, Lisbon, Portugal
mekal@isr.tecnico.ulisboa.pt

Rodrigo Ventura

Institute for Systems and Robotics
Instituto Superior Técnico
Avenida Rovisco Pais 1, Lisbon, Portugal
rodrigo.ventura@isr.tecnico.ulisboa.pt

Richard Linares

Department of Aeronautics and Astronautics
Massachusetts Institute of Technology
77 Massachusetts Avenue, Cambridge, MA 02139
linaresr@mit.edu

Abstract

On-orbit close proximity operations involve robotic spacecraft maneuvering and making decisions for a growing number of mission scenarios demanding autonomy, including on-orbit assembly, repair, and astronaut assistance. Of these scenarios, on-orbit assembly is an enabling technology that will allow large space structures to be built in-situ, using smaller building block modules. However, like many of these scenarios, robotic on-orbit assembly involves a number of technical hurdles such as changing system models. For instance, grappled modules moved by a free-flying “assembler” robot can cause significant shifts in system inertial properties, which has cascading impacts on motion planning and control portions of the autonomy stack. Further, on-orbit assembly and other scenarios require collision-avoiding motion planning, particularly when operating in a “construction site” scenario of multiple assembler robots and structures. These complicating factors, relevant to a number of autonomous microgravity robotics use cases, are tackled in the ReSWARM flight experiments as a set of tests on the International Space Station using NASA’s Astrobee robots. RELative Satellite sWarming and Robotic Maneuvering, or ReSWARM, demonstrates multiple key technologies for close proximity operations, and on-orbit assembly in particular: (1) global long-horizon planning, accomplished using offline and online sampling-based planner options that consider the system dynamics; (2) on-orbit reconfiguration model learning, using the recently-proposed RATTLE information-aware planning framework; and (3) robust control tools to provide low-level control robustness using current system knowledge.

*Equal contribution.

These approaches are detailed individually and in an “on-orbit assembly scenario” of multi-waypoint tracking on-orbit. Additionally, significant operational and implementation detail is provided discussing the practicalities of hardware implementation and unique aspects of working with the Astrobees free-flyer robots in microgravity. ReSWARM provides a base set of planning and control tools for robotic close proximity operations, demonstrates them in microgravity, and outlines some of the important hardware aspects that future autonomous free-flyers will need to consider.

1 Introduction

On-orbit robotic assembly and servicing of large, complex space structures is an emerging area of autonomy that can improve space-borne observatories, communications relays, and human space exploration among other areas. On-orbit servicing is a superset of areas including repairing, refueling, and re-provisioning of spacecraft (Saleh et al., 2003). For instance, there are currently many Earth observing satellites investigating the Earth’s oceans and land masses (e.g. Landsat-7 (Goward et al., 2001)), whose longevity could be increased by on-orbit servicing and assembly. Specifically, new servicing and assembly technologies are being developed through NASA’s On-orbit Servicing, Assembly, and Manufacturing 1 (OSAM-1) servicing mission which will refuel Landsat-7 (Reed et al., 2016; Coll et al., 2020).

Concepts in the area of robotic assembly of space structures have also been proposed by industry and academia. Tethers Unlimited, Inc. is enabling the area of on-orbit fabrication including antennas, solar panels, and truss structures using SpiderFab (Hoyt, 2013). Made In Space, Inc. is developing the manufacturing and assembly of spacecraft components on-orbit using its Archinaut One concept (Patane et al., 2017). These assemblers are defined by capturing the structure with a robotic arm and climbing the structure for servicing or construction. Alternatively, space structures can be assembled using proximity operations with free-flyer robots, providing benefits in terms of mission flexibility and range of motion (Jewison et al., 2014). MIT’s Space Systems Laboratory (SSL) has used the Astrobees (Bualat et al., 2015) and SPHERES robots—six degree of freedom (DOF) robotic free-flyers operating aboard the International Space Station (ISS)—to develop capabilities relating to autonomy, multi-agent coordination, and microgravity manipulation (Doerr et al., 2021; Ekal et al., 2021; Miller et al., 2000). Recently, Astrobees has begun operations to replace the SPHERES satellites, providing the functionality necessary to demonstrate capabilities in modular motion planning strategies for on-orbit assembly. By enabling the autonomous robotic assembly of space structures and more, on-orbit assembly serves as a useful scenario for other on-orbit autonomy domains including servicing. The sum total of these emerging areas of microgravity robotic autonomy will lead to improved science-gathering (e.g. upgrading new components), mission life extension (e.g. repairing, refueling, and re-provisioning), and other benefits. As such, with the growing availability of on-orbit general-purpose computing power and robotic platforms, the desire to apply autonomy to these scenarios becomes appealing from an efficiency and safety standpoint.

This work addresses the motion planning and control for on-orbit robotic assembly in the presence of inertial parametric uncertainty caused by payload manipulation using an online, adjustable information-aware planning algorithm. Although inertial properties of the payload (e.g. 3D printed parts) may be known, the manipulated system (i.e. the 3D printed part and robotic assembler system) may have inertial parametric uncertainty due to uncertainties in which the payload is grasped. Having an online, adjustable information-aware planning algorithm is a necessary component to many on-orbit robotic autonomy mission scenarios and the method builds upon a previously proposed motion planning and control framework which used offline-computed informative paths to mitigate uncertainty caused by payload manipulation (Doerr et al., 2021). Building on this prior work, microgravity experimental results using the Astrobees robotic free-flyer are presented in this context for the first time. Test cases which are representative of on-orbit proximity operations such as payload transportation and assembly are considered under the following steps. First, a spacecraft (Astrobees) collects a payload. This results in an increase in inertial uncertainty of the spacecraft system. Next, the spacecraft mitigates the inertial uncertainty using online information-aware planning and

estimation. Finally, the spacecraft precisely deposits the payload in its designated location. A number of planning and control methods, repurposable to other on-orbit autonomy tasks, are discussed in terms of these test cases; techniques include high-level motion planning with obstacle avoidance, robust tube model predictive control (MPC), and online inertial model learning. Implementation on the Astrobees hardware provides lessons learned for the field testing of these motion planning and control techniques in a microgravity robotic system with processing capabilities similar to that of emerging space robotic systems. Algorithmically, a safe and uncertainty-aware design for the assembling of space structures on-orbit is provided which can be expanded to constructing next generation telescopes, space stations, and communication satellites.

Statement of Contributions: This work provides a number of contributions, focusing on practical application and field testing of motion planning and control to on-orbit autonomy relevant for robotic free-flyers:

- Providing motion planning and control components for microgravity robotic free-flyer autonomy, with novel enhancements beyond (Doerr et al., 2021) including online information-aware planning and an alternative real-time global planner, among others.
- Demonstration of the above for an on-orbit payload transportation use case scenario in microgravity experiments, including individual demonstrations of each major planning/control component over a series of two ISS experiments.
- Discussion of extensive hardware implementation details and challenges emerging from field testing, with suggestions for general implementation on other systems.

The paper is organized as follows. Section 2 discusses relevant prior work for microgravity robotic autonomy; Section 3 describes the formulation of the essential planning under uncertainty problem with practical implications for running on hardware; Section 4 explores key methods and techniques in addressing the problem formulation; Subsection 4.6 reveals two planning and control architectures for addressing the problem; Section 6 details the on-orbit experimental results of these architectures during the ReSWARM-1 and ReSWARM-2 ISS test sessions; finally, Section 7 provides discussion and concluding remarks of the hardware-demonstrated methods and future work.

2 Related Work

The on-orbit assembly problem touches on multiple areas of active areas of work in the robotics and space systems literature, including real-time motion planning, planning and control under uncertainty, and online system identification. Since on-orbit assembly involves autonomous manipulation of payloads, surveying, robotic locomotion, and safety planning/control it is inherently a robotics problem with unique considerations because of the safety-critical nature of its operating environment. This section addresses these broad areas of research in the robotics literature, highlighting topics which are most relevant to the on-orbit assembly problem.

2.1 On-Orbit Assembly

The autonomous on-orbit assembly problem concerns multiple topics, including mission concepts (Gralla and De Weck, 2007; Izzo et al., 2005), path planning (Badawy and McInnes, 2008) as well as control of assembly vehicles and components (McInnes, 1995; McQuade and McInnes, 1997). Works such as (Shi et al., 2016) have addressed the issue of change in inertial parameters during assembly, and designed robust control approaches to deal with this. In contrast, this work considers a free-flyer satellite tasked with carrying components to their assembly location. Optimal and dynamically feasible motion plans are determined and tracked with robust control, while the change in inertial properties from grappling payload is addressed through information-aware motion planning and subsequent parameter estimation.

Aside from progress in on-orbit assembly, significant developments have been made in assembly of structures in terrestrial environments. Specifically, modular control strategies utilizing component geometry have been developed to build structures using ground and aerial robotics (Petersen et al., 2011; Willmann et al., 2012). Collaborative multi-robotic systems have also been designed to transport and manipulate voxels to construct plates, enclosures, and cellular beams (Jenett et al., 2019) and through coarse and fine manipulation techniques (Dogar et al., 2015). Distributed control has been used for larger multi-robotic systems so agents can collectively climb and assemble the structure they are building (Werfel et al., 2014). Likewise, a number of architectures have been proposed for on-orbit assembly strategies. Superquadric potential fields have been applied to assemble components of a structure while providing collision avoidance (Badawy and McInnes, 2008). Other methods focus on the specifics of the planning and control stacks required, including innovative techniques from terrestrial robotics such as sampling-based motion planners, nonlinear model predictive control (NMPC), and many others (Perez et al., 2012; Geraerts and Overmars, 2007; Sathya et al., 2018; Doerr and Linares, 2020).

2.2 Robotic Motion and Path Planning

Ground (terrestrial) robotics has provided technological advancements in motion planning and trajectory optimization, which is the foundation necessary to autonomously assemble structures. Gradient-based optimization techniques like the Covariant Hamiltonian Optimization for Motion Planning (CHOMP) (Ratliff et al., 2009) have been popularized for optimal trajectory planning under constraints, constructing near-optimal trajectories based on the cost, dynamics, and obstacle constraints from an initial and possibly unfeasible trajectory. However, even with gradient information such techniques may get stuck in local minimums or suffer under sufficiently complex/cluttered environments and dynamics. Numerically robust and computationally efficient methods to trajectory optimization have been achieved through the use of sequential convex programming (SCP), such as TrajOpt and GuSTO (Schulman et al., 2013) (Bonalli et al., 2019). Such methods use sequential convex programming (SCP) to numerically optimize L_1 distance penalties for both inequality and equality constraints, solving an approximate convex problem using sequential quadratic programming, sometimes incorporating guarantees from optimal control. A computationally simpler algorithm to SCP is the proximal averaged Newton-type method for optimal control (PANOC) algorithm (Stella et al., 2017). The PANOC optimizer is a line-search method that integrates Newton-type steps and forward-backward iterations over a real-valued continuous merit function, achieving fast convergence using first-order information of the cost function and a reduction in matrix operations when compared to SCP (Stella et al., 2017; Sathya et al., 2018).

Another possible set of approaches are gradient-free, like Stochastic Trajectory Optimization for Motion Planning (STOMP) (Kalakrishnan et al., 2011). Since STOMP uses no gradient information, costs that are non-differentiable and non-smooth can still be used to find optimal trajectories; however, optimizing trajectories with this technique is inefficient compared to CHOMP and gradient-based approaches because of the loss of cost function information.

Other major planning approaches include the sampling-based planners (SBP). Among them, the rapidly exploring random tree (RRT) and RRT* may be adapted to plan dynamically feasible trajectories (Karaman and Frazzoli, 2011). These algorithms produce probabilistically complete solutions, and their optimizing forms contain asymptotically optimal motion planning solutions. Historically, the cost-to-go heuristic for optimizing variants has been a Euclidean distance metric to minimize the L_2 distance, but this has been improved to reflect the dynamics and control of systems using cost-to-go pseudo-metric like that of the linear quadratic regulator (LQR) (Perez et al., 2012). The advantage of RRT*-based algorithms is that they can be applied to real-time systems in a computationally efficient manner in which the sampling itself can be interrupted at set time-intervals to allow for real-time operation as well as providing explicit collision-checking for collision-free trajectories.

2.3 Motion Planning under Uncertainty and Model Improvement

Uncertainty can be caused by effects intrinsic to the system (e.g., unmodeled dynamics, sensor noise, etc.), or external sources (e.g., disturbances like wind, solar pressure, etc.). As robotic systems and the tasks that they are entrusted with get increasingly complex, dealing with this uncertainties has become key to many motion planning schemes. Some of these uncertainties are parametric and can be learned through explicit action of the robotic system; others are unstructured, providing disturbance terms that must be countered through control or replanning. Model-based control, path planning and control with optimal fuel or energy consumption, behaviour prediction, and fault detection are just some situations that require are touched upon by introduction of uncertainty into the model; parametric uncertainty reduction (e.g., moments of inertia), also serves to benefit many of these areas. This is especially relevant for on-orbit assembly operations, where robotic free-flyers would need to precisely and safely transport various uncertain components to their assembly locations while dealing with unstructured uncertainties.

Approaches for inertial uncertainty reduction can be classified into three broad groups based on whether the learned inertial properties are used in planning and control. The first approach is the use of system identification, where optimal excitation design is used to adequately characterise the system. The estimated parameters are then used by the controller for precise task execution. The Newton-Euler equations of motion, or the equations of angular momentum conservation are often a starting point for formulating the estimation problem (Keim et al., 2006; Ma et al., 2008; Rackl et al., 2013; Wilsona et al., 2004; Yoshida and Abiko, 2002).

The second approach can be termed as disturbance rejection, where the effects of uncertainty are treated as bounded, unwanted disturbances, and control algorithms are designed to execute tasks despite them. Robust model predictive control, the use of funnel libraries, direct adaptive control and model-free reinforcement learning can be classified as disturbance-rejecting (Mayne et al., 2005; Lopez et al., 2019; Majumdar and Tedrake, 2017; Wu et al., 2020).

The third group of methods can be addressed as simultaneous learning, where the parameters are learned online and the updated parameters are used in planning and control. In case learning the system parameters is relevant for the task at hand, simultaneous learning approaches can potentially reduce the time and energy consumed by a full system identification, while at the same time also completing the robot's primary task without being too conservative. Indirect adaptive control, learning-based model predictive control, model-based reinforcement learning and active learning techniques fall under this category (Espinoza and Roascio, 2017; Ostafew et al., 2016; Slade et al., 2017; Webb et al., 2014; Albee et al., 2022).

The principle of active learning or optimal experimental design is to choose data from which to learn, in order to obtain a greater degree of accuracy and efficiency in the learning process (Settles, 2009). For instance, information-seeking motion plans are often used in conjunction with parameter or state estimation algorithms with the goal of gathering information-rich measurements to improve estimation accuracy. Depending on how the objective is formulated, active-learning approaches could be implicit or explicit. Most implicit class of methods solve an approximation of the stochastic optimal control problem. The resulting control policy is thus inherently information-seeking. Examples are work on POMDPs with covariance minimization (Webb et al., 2014) and covariance steering (Okamoto and Tsiotras, 2019). These approaches have not yet been implemented on hardware and their scalability remains an issue. Explicit active learning approaches incentivize information seeking behaviour, for instance using metrics such as Fisher information (Wilson and Murphey, 2015).

Machine learning tools such as Gaussian process regression have been used in literature for disturbance modeling (Ostafew et al., 2016) or for learning non-linear system models (Lee et al., 2017). For learning inertial parameters, batch or recursive least square methods can be used, provided an estimation problem linear in terms of the estimates can be formulated or approximated, and that information rich exciting trajectories are used to ensure that the regressor is full-rank and invertible (Keim et al., 2006; Yoshida and Abiko, 2002), or non-linear least squares optimization can be used. In these cases, (Wensing et al., 2017)

provides a formulation for enforcing physical feasibility constraints on the estimates. Sequential filtering methods such as the Kalman Filter or Unscented Kalman Filter can be used for either parameter estimation, or joint estimation of states and parameters (Lichter and Dubowsky, 2004; VanDyke et al., 2004).

2.4 Model Predictive Control

Model predictive control (MPC) is a control technique which is particularly notable for its ability to approximately optimally control general dynamical systems under constraints. Model predictive control’s used is widespread in robotics due to its modeling flexibility and, recently, its ability to be used in real-time and sometimes with mathematical guarantees on performance. While proofs for MPC stability under certain conditions (Mayne et al., 2011) exist, guarantees for stochastic systems are generally lacking. Tube MPC is a notable exception, providing robustness guarantees when bounded additive uncertainty is encountered in the system dynamics (Raković and Levine, 2019). Safety guarantees for control are also emerging in other forms, such control barrier functions and reachable set analysis (Lopez et al., 2020) (Majumdar and Tedrake, 2017) (Brunke et al., 2021) (Singh et al., 2017).

Tube MPC is a flexible robust control approach for handling unstructured uncertainty. With Tube MPC, a portion of control authority is reserved for robust actuation, often in a simple feedback form to counter disturbances. The guarantee obtained is one of tube robustness—if a system starts in a tube of possible states, it remains within a tube around a nominal trajectory. These tubes are formed around the nominally planned MPC trajectory, and the motion of the system can be thought of as a composition of these planned “safe sets”. Tube MPC methods exist for both nonlinear (Lopez, 2019) and linear (Limon et al., 2008) systems with additive bounded uncertainty—for the on-orbit assembly problem linear tube MPC is of interest for the linear translational satellite (double integrator) dynamics. In essence, two controllers must be produced: (1) a nominal MPC, operating under a modified set of constraints to account for worst-case uncertainty; (2) an ancillary or “disturbance rejection” controller that provides robustness to aleatoric uncertainty. Given a reference trajectory, tube MPC will repeatedly plan the nominal trajectory online, and append ancillary controller actuation to the system inputs, resulting in tube robustness.

3 Problem Formulation

The on-orbit assembly problem is now framed for a microgravity free-flyer robotic system. The discussion here highlights this particular robotic system since it has broad applicability to on-orbit assembly problems, serving as a highly mobile robotic base that can grapple and move payloads, observe structures, and more. The key uncertainty sources are introduced—primarily inertial uncertainty for close proximity operations/on-orbit assembly scenarios—and the distinctions between two main types of uncertainty are made. Finally, a sketch of the on-orbit assembly task used for on-orbit experimentation is outlined.

3.1 System Dynamics and Introducing the Motion Planning Problem

A free-flyer must move from \mathbf{x}_0 to \mathbf{x}_f , with continuous-time nonlinear dynamics given by

$$\dot{\mathbf{x}}(t) = f(\mathbf{x}(t), \mathbf{u}(t), \boldsymbol{\theta}(t)), \quad (1)$$

where $\mathbf{x}(t) \in \mathbb{R}^{n_x}$ is the robot state, $\mathbf{u}(t) \in \mathbb{R}^{n_u}$ is the robot control input, and $\boldsymbol{\theta}(t) \in \mathbb{R}^{n_\theta}$ is an uncertain parameter vector about time t and where n_x , n_u , and n_θ are the sizes of the state, control, and inertia parameter vectors, respectively. The free-flyer robotic system is described about a full 6 degree of freedom (DOF) in translation and rotational motion. The system can be controlled about the 6 DOF with the necessary forces and torques applied to the robot. The inertial parameters contain both the mass and moments of inertia of the system.

The dynamics are depicted in Fig. 1. A large portion of uncertainty in this scenario is epistemic (see Section 3.2)—there is a good system model and the parameters are learnable. (Note that the free-flying dynamics (Dubowsky and Papadopoulos, 1993) are a possible addition, though for now this work considers only the rigid body dynamics without a manipulator arm.) The dynamics are the Newton-Euler equations about the center of mass (cm) given by

$$\begin{aligned} \mathbf{r} &= [r_x \ r_y \ r_z]^\top \\ \mathbf{q} &= [q_x \ q_y \ q_z \ q_\theta]^\top \\ \mathbf{v} &= [v_x \ v_y \ v_z]^\top \\ \boldsymbol{\omega} &= [\omega_x \ \omega_y \ \omega_z]^\top \end{aligned} \quad \mathbf{x} = \begin{bmatrix} \mathbf{r} \\ \mathbf{q} \\ \mathbf{v} \\ \boldsymbol{\omega} \end{bmatrix} \quad (2)$$

$$\begin{aligned} \dot{\mathbf{r}}_{cm} &= \mathbf{v} \\ \dot{\mathbf{v}}_{cm} &= \frac{\mathbf{F}}{m} \\ \dot{\boldsymbol{\omega}} &= -\mathbf{I}^{-1}\boldsymbol{\omega} \times \mathbf{I}\boldsymbol{\omega} + \mathbf{I}^{-1}\boldsymbol{\tau} \\ \dot{\mathbf{q}}_{IB} &= \frac{1}{2}\bar{H}(\mathbf{q}_{IB})^\top{}^B\boldsymbol{\omega}_{IB}. \end{aligned} \quad (3)$$

This may also be written in matrix form for a 6 DOF rigid body expressed in a body-fixed frame not coincident with the centre of mass (CM),

$$\begin{bmatrix} \mathbf{F} \\ \boldsymbol{\tau}_{CM_0} \end{bmatrix} = \begin{bmatrix} m\mathbf{I}_3 & -m[\mathbf{c}]_\times \\ m[\mathbf{c}]_\times & \mathbf{I}_{CM} - m[\mathbf{c}]_\times[\mathbf{c}]_\times \end{bmatrix} \begin{bmatrix} \dot{\mathbf{v}} \\ \dot{\boldsymbol{\omega}} \end{bmatrix} + \begin{bmatrix} m[\boldsymbol{\omega}]_\times[\boldsymbol{\omega}]_\times\mathbf{c} \\ [\boldsymbol{\omega}]_\times(\mathbf{I}_{CM} - m[\mathbf{c}]_\times[\mathbf{c}]_\times)\boldsymbol{\omega} \end{bmatrix}, \quad (4)$$

where $\mathbf{v}, \boldsymbol{\omega} \in \mathbb{R}^3$ denote the linear velocity and angular velocity of the original center of mass (CM₀), \mathbf{I}_{CM} is the inertia tensor about the CM, m is the system mass, and $\mathbf{c} \in \mathbb{R}^3$ is the CM offset from CM₀. $\mathbf{F}, \boldsymbol{\tau} \in \mathbb{R}^3$ are the forces and torques applied through the \mathcal{F}_B body frame, where \mathcal{F} indicates the inertial reference frame (Ekal et al., 2021). $[-]_\times$ is used to indicate a cross product matrix.

The inertia tensor \mathbf{I} is given fully as

$$\mathbf{I} = \begin{bmatrix} I_{xx} & I_{xy} & I_{xz} \\ I_{yx} & I_{yy} & I_{yz} \\ I_{zx} & I_{zy} & I_{zz} \end{bmatrix}. \quad (5)$$

The inertia tensor may often be assumed to be diagonal if the principal axes are aligned with the base frame, resulting in the diagonal principal moments of inertia $\{I_{xx}, I_{yy}, I_{zz}\}$.¹

To develop the motion planning and control for hardware testing, discrete dynamics are defined and also require linear time-varying (LTV) system approximations. First, a first-order Taylor series expansion about

¹Further, it may be shown that only the ratios of the principal moments of inertia (such that \mathbf{I} is diagonal) need be known for Euler's equations: $p_x = \frac{I_{yy}-I_{zz}}{I_{xx}}$, $p_y = \frac{I_{zz}-I_{xx}}{I_{yy}}$, and $p_z = \frac{I_{xx}-I_{yy}}{I_{zz}}$.

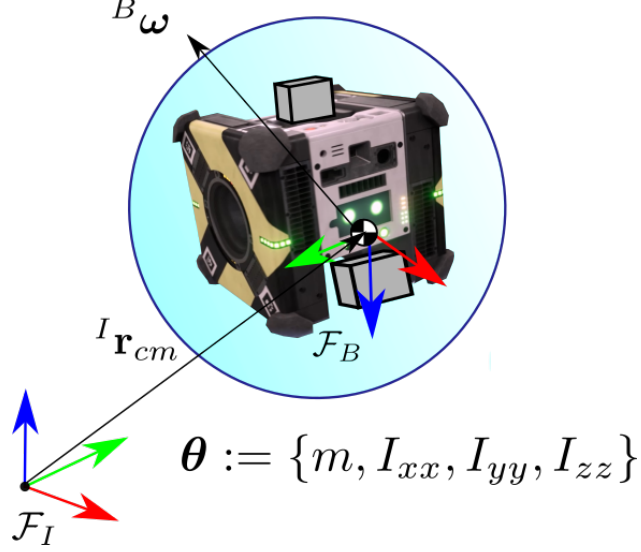


Figure 1: The Newton-Euler dynamics with parameters of interest for the cargo maneuvering scenario.

an operating point for linearization is determined (Markley and Crassidis, 2014), and then, discretization using a fourth-order Runge-Kutta method with a zero-order hold on control is applied (Van Loan, 1978). This results in an LTV system given by

$$\delta \mathbf{x}_{k+1} = A_k \delta \mathbf{x}_k + B_k \delta \mathbf{u}_k, \quad (6)$$

where A_k and B_k are the state and control matrices at a time-step k . The terms $\delta \mathbf{x}_k = (\mathbf{x}_k - \bar{\mathbf{x}}_k)$ and $\delta \mathbf{u}_k = (\mathbf{u}_k - \bar{\mathbf{u}}_k)$ are the perturbation state and control about some operating point $\bar{\mathbf{x}}_k$. For this work, the operating point occurs at some target $\bar{\mathbf{x}}_k = \mathbf{x}_{des}$.

Ideally, this system will also obey some sort of optimality in its motion, which can be captured in an objective function. The objective of the nominal system (ignoring parametric uncertainty) is to plan and control the robotic free-flyer using a quadratic cost function

$$J(\delta \mathbf{x}_0, \delta U_{0:N-1}) = \sum_{k=0}^{N-1} l(\delta \mathbf{x}_k, \delta \mathbf{u}_k) + l_N(\delta \mathbf{x}_N), \quad (7)$$

where $\delta U_{0:N-1} = [\delta \mathbf{u}_0, \delta \mathbf{u}_1, \dots, \delta \mathbf{u}_{N-1}]$ is the control sequence, $l(\delta \mathbf{x}_k, \delta \mathbf{u}_k)$ is the running cost, and $l_N(\delta \mathbf{x}_N)$ is the terminal cost to a time N . This is given by

$$l(\delta \mathbf{x}_k, \delta \mathbf{u}_k) = \frac{1}{2} \begin{bmatrix} 1 \\ \delta \mathbf{x}_k \\ \delta \mathbf{u}_k \end{bmatrix}^T \begin{bmatrix} 0 & \mathbf{q}_k^T & \mathbf{r}_k^T \\ \mathbf{q}_k & Q_k & P_k \\ \mathbf{r}_k & P_k & R_k \end{bmatrix} \begin{bmatrix} 1 \\ \delta \mathbf{x}_k \\ \delta \mathbf{u}_k \end{bmatrix}, \quad l_N(\delta \mathbf{x}_N) = \frac{1}{2} \delta \mathbf{x}_N^T Q_N \delta \mathbf{x}_N + \delta \mathbf{x}_N^T \mathbf{q}_N, \quad (8)$$

where \mathbf{q}_k , \mathbf{r}_k , Q_k , R_k , and P_k are the running weights (coefficients), and Q_N and \mathbf{q}_N are the terminal weights. The weight matrices, Q_k and R_k , are positive definite and the block matrix $\begin{bmatrix} Q_k & P_k \\ P_k & R_k \end{bmatrix}$ is positive-semidefinite (Inaba and Corke, 2016). This is constrained to dynamics and obstacles (structural components) of the assembly problem itself.

Constraints for the Free-Flyer On-Orbit Assembly Scenario The constraint sets \mathcal{X} and \mathcal{U} define permissible values for \mathbf{x} and \mathbf{u} . For both \mathbf{x} and \mathbf{u} , the constraints of interest are

$$\text{position: } \mathbf{r} \in \mathcal{X}_{module} \tag{9}$$

$$\text{velocity: } \mathbf{v}_{max} < \mathbf{v} < \mathbf{v}_{max} \tag{10}$$

$$\text{angular velocity: } -\boldsymbol{\omega}_{max} < \boldsymbol{\omega} < \boldsymbol{\omega}_{max} \tag{11}$$

$$\text{force input: } \mathbf{f} < \mathbf{f}_{max} \tag{12}$$

$$\text{torque input: } \boldsymbol{\tau} < \boldsymbol{\tau}_{max} \tag{13}$$

where the position/obstacle constraint $\mathbf{r} \in \mathcal{X}_{module}$ is confined about the experimental module with obstacles and must be enforced by a form of collision-checker, as mentioned in Section 4.2. Note that the input constraints are significantly complicated by the coupled nature that inputs are applied through the system’s mixer (Jewison, 2014). A simplifying assumption is to make each respective constraint small enough that force and torque can independent saturate and not cause individual thruster saturations.

3.2 Forms of Model Uncertainty and the Stochastic Planning Problem

A robotic system has a state vector, $\mathbf{x} \in \mathbb{R}^n$ which describes its configuration. A nominal, deterministic model, \mathcal{M} governs how this state vector evolves,

$$\mathcal{M} : \{\mathbf{x}, \mathbf{u}\} \in \mathbb{R}^n, \mathbb{R}^m \rightarrow \mathbf{x} \in \mathbb{R}^n \tag{14}$$

where inputs $\mathbf{u} \in \mathbb{R}^m$ are available to influence the system’s motion. A mobile robotic system, like a free-flyer transporting payload, will experience uncertainty in its motion model in two broad forms: parametric and unstructured uncertainty. While deterministic models are very useful for proposing nominal solutions to planning and control problems—as in the discussion of the prior section—they do not adequately capture one’s knowledge of the model. Uncertainty enters the problem in one of two ways:

- **Epistemic:** Systematic uncertainty, due to information that could be known, but is not in practice. It is a design decision whether or not to incorporate or improve this information.
- **Aleatoric:** Statistical uncertainty, due to unknowns that vary each time an experiment is run. It is considered beyond modeling capability.

Uncertain parameters are a common form of epistemic uncertainty, represented by a parameter vector $\boldsymbol{\theta} \in \mathbb{R}^{n_\theta}$. It is necessary to describe knowledge of these parameters in some way—a belief (a probability distribution) is frequently assigned to the parameters to describe the current level of knowledge,

$$\boldsymbol{\theta} \sim \mathcal{N}(\bar{\boldsymbol{\theta}}, \boldsymbol{\Sigma}_\theta) \tag{15}$$

where $\bar{\boldsymbol{\theta}}$ is the most likely belief value—the center of the Gaussian distribution—and $\boldsymbol{\Sigma}_\theta$ is the parameter covariance matrix. A Gaussian has been selected as the parameter belief representation, a common assumption in the literature for a variety of reasons.² Gaussians will frequently be used as the assumed belief state throughout this problem formulation and thesis, though it is possible to use other distributions if desired.

²Among these are the Central Limit Theorem implying that Gaussians are often a good choice for poorly understood distributions and convenient propagation properties of Gaussians (i.e., linear transformations of Gaussians are also Gaussians).

Uncertain parameters are constant but unknown values with a known functional form in the system dynamics model. The dynamics model with parametric uncertainty becomes

$$\dot{\mathbf{x}} = f(\mathbf{x}, \mathbf{u}, \boldsymbol{\theta}) \quad (16)$$

equivalent to the dynamics of equation 1 where parametric uncertainty is considered. There is a ground truth value for these unknowns but the system does not start off with exact knowledge of the parameters' ground truth values, instead relying on an initial belief for the parameter(s), $\mathcal{N}(\hat{\boldsymbol{\theta}}_0, \boldsymbol{\Sigma}_{\theta,0})$. In the case where epistemic uncertainty is not learned, for all intents and purposes this uncertainty is aleatoric, where \mathbf{w}_x (the additive uncertainty, or noise) is entirely the result of having an inadequate understanding of model parameters. The system under pure noise uncertainty would look similar, except the uncertainty would not be considered to be caused by parametric unknowns that are not learned, but rather by unknowable disturbance sources like environmental perturbations, for instance (perhaps the robot gets jostled a bit while traversing the construction site.). For the full aleatoric system with constraints, the complete motion planning problem is

$$\begin{aligned} \min_{\mathbf{u}(t)} J &= \mathbb{E} \left[\int_{t_0}^{t_f} l(\mathbf{x}(t), \mathbf{u}(t)) dt + l_N(\mathbf{x}(t_f), \mathbf{u}(t_f)) \right] \\ l(t) &= \mathbf{x}(t)^\top \mathbf{Q} \mathbf{x}(t) + \mathbf{u}(t)^\top \mathbf{R} \mathbf{u}(t) \\ l_N(t) &= \mathbf{x}(t_f)^\top \mathbf{H} \mathbf{x}(t_f) \\ \text{such that} & \\ \dot{\mathbf{x}} &= \mathbf{A} \mathbf{x}(t) + \mathbf{B}(\boldsymbol{\theta}) \mathbf{u}(t) + \mathbf{w}_x \\ \mathbf{w}_x &\sim \mathcal{N}(0, \boldsymbol{\Sigma}_w) \\ \mathbb{E} [\mathbf{x}(t_0)] &\sim \mathcal{N}(\bar{x}_0, \boldsymbol{\Sigma}_{x,0}) \\ u &\in \mathcal{U} \\ x &\in \mathcal{X}_{free} \end{aligned} \quad (17)$$

The parameter(s) may be updated enroute if new information characterizing the belief state becomes available. (The noise, \mathbf{w}_x , may also be updated if the noise process is better characterized.) The parameter(s) $\boldsymbol{\theta}$ may therefore be thought of as a form of epistemic (resolvable uncertainty), while \mathbf{w}_x is still a form of aleatoric (inherent, unresolvable) uncertainty. Note that the cost function is now over an expectation of accumulated cost due to the uncertain model of the system. This is a stochastic, constrained, trajectory optimization problem which in practice is challenging to obtain optimal solutions for. However, a common approach in robotics and controls is assuming a known, zero-mean, Gaussian additive disturbance on the system dynamics, and providing robust or probabilistically robust (i.e., chance-constrained) means of planning and control. However, such approaches frequently overlook the *dual control* problem—that is, acknowledging that these uncertainties can sometimes be better understood *online*, as the system executes. Even in this case, for a limited set of systems, optimal solutions can be found; for instance, the stochastic HJB equation leads to the famous linear quadratic Gaussian (LQG) for this system (without constraints).

Model Parameters and Parametric Uncertainty of the Free-Flyer System Returning to the on-orbit assembly free-flyer dynamics, the full parameter vector containing all inertial property uncertainty may be written as

$$\boldsymbol{\theta} \triangleq [m, I_{xx}, I_{yy}, I_{zz}, I_{xy}, I_{xz}, I_{yz}, \mathbf{r}_{CM}^\top]^\top. \quad (18)$$

A simplifying assumption that approximates model changes for cargo maneuvering tasks that the Astrobeer robot might frequently encounter considers CM offset negligible. This simplification also aids the parameter estimation and planning tasks by reducing $|\boldsymbol{\theta}|$. The model’s parameters, assuming negligible center of mass change and known principal axes, are then

$$\boldsymbol{\theta} \triangleq [m, I_{xx}, I_{yy}, I_{zz}]^\top, \tag{19}$$

where each of which has an associated initial belief, $\theta_i \sim \mathcal{N}(\bar{\theta}_i, \sigma_{\theta,i})$. It is assumed the uncertainty is primarily due to the unknown parameters $\boldsymbol{\theta}$, but additive noise, \mathbf{w} , is also possible.

3.3 The On-Orbit Assembly Scenario

The on-orbit assembly scenario considers the stochastic motion planning problem for a robotic free-flyer of the prior section, where portions of the scenario might benefit from online parametric model updating. For the on-orbit assembly scenario, three types of planning and control maneuvers are areas of interest. The first area of interest is the use of offline planning that can be produced in passive waiting areas. In this case, the system model knowledge is considered adequate and robust tracking is unnecessary. The second area of interest is the use of online planning, control, and estimation that is responsive to poor model knowledge and has a time sensitivity. Therefore, real-time plans are desirable. Lastly, offline planning that can be produced in passive waiting areas with adequate system model knowledge is considered. In this case there is uncertainty that makes robust tracking desirable. The experimental setup of the on-orbit assembly scenario is covered in greater detail in Section 5; the next section introduces the methods and approaches to cover these areas.³

4 Methods and Approach

The on-orbit assembly planning and control problem is tackled through a tiered combination of global and local planning and low-level control. Additionally, information-aware and robust planning and control methods are deployed in some portions of the stack to aid in dealing with system uncertainty. First, the methods deployed are introduced, followed by their composition as a suite of on-orbit assembly under uncertainty tools.

4.1 Dynamics-Aware and Real-Time Global Planning Methods

The motion planning for on-orbit assembly using a free-flyer is developed using RRT* based methods including LQR-RRT* and kinodynamic RRT. Additionally, trajectory smoothing using LQR shortcutting is used to find shortcut trajectories based off the initial sample-based trajectory. The motivation of using sampling-based motion planning is that it provides computationally efficient, collision-free trajectories through random sampling of the complex state-space (Perez et al., 2012). In literature, LQR-RRT* and trajectory smoothing have been discussed extensively (Paden et al., 2016; Geraerts and Overmars, 2007; Kallmann et al., 2008). In this work, LQR-RRT* and trajectory smoothing using LQR shortcutting are discussed with application to on-orbit assembly using free-flyers which follows from previous work (Perez et al., 2012; Doerr and Linares, 2020).

³A portion of these methods are also documented in the thesis (Albee, 2022).

4.1.1 Optimizing Global Planning Module: LQR-RRT*

For a nonlinear system given in Eq. (3), the goal is to obtain a trajectory that minimizes the quadratic cost function given in Eqs. (7) and (8) with initial and final states, \mathbf{x}_0 and \mathbf{x}_{des} , respectively. The quadratic cost is simplified to

$$J(\delta\mathbf{x}_0, \delta U_{0:N-1}) = \sum_{k=0}^{N-1} \delta\mathbf{x}_k^T \mathbf{q}_k + \delta\mathbf{u}_k^T \mathbf{r}_k + \frac{1}{2} \delta\mathbf{x}_k^T Q_k \delta\mathbf{x}_k + \frac{1}{2} \delta\mathbf{u}_k^T R_k \delta\mathbf{u}_k + \delta\mathbf{u}_k^T P_k \delta\mathbf{x}_k + \frac{1}{2} \delta\mathbf{x}_N^T Q_N \delta\mathbf{x}_N + \delta\mathbf{x}_N^T \mathbf{q}_N. \quad (20)$$

The optimal solution with respect to the cost function in terms of the control sequence is given by

$$\delta U_{0:N-1}^*(\delta\mathbf{x}_0) = \arg \min_{\delta U_{0:N-1}} J(\delta\mathbf{x}_0, \delta U_{0:N-1}). \quad (21)$$

To solve for the control solution in Eq. (21), a value iteration is used which determines the optimal cost-to-go (value) starting from the final time-step and moving backwards in time minimizing the control sequence. This is given by

$$J(\delta\mathbf{x}_k, \delta U_{k:N-1}) = \sum_k^{N-1} l(\delta\mathbf{x}_k, \delta\mathbf{u}_k) + l_N(\delta\mathbf{x}_N), \quad (22a)$$

$$V(\delta\mathbf{x}_k) = \min_{\delta U_{k:N-1}} J(\delta\mathbf{x}_k, \delta U_{k:N-1}), \quad (22b)$$

which is similar to Eq. (7) and Eq. (21), but the cost starts from time-step k instead. The optimal cost-to-go at time-step k is a quadratic function given by

$$V(\delta\mathbf{x}_k) = \frac{1}{2} \delta\mathbf{x}_k^T S_k \delta\mathbf{x}_k + \delta\mathbf{x}_k^T \mathbf{s}_k + c_k, \quad (23)$$

where S_k , \mathbf{s}_k , and c_k are computed backwards in time from the final conditions $S_N = Q_N$, $\mathbf{s}_N = \mathbf{q}_N$, and $c_N = c$. Thus, the minimization of the control sequence becomes a minimization over a control input at a time-step which is known as the principle of optimality (Bellman et al., 1954). To find the optimal value, the Ricatti equations are propagated backwards from the final conditions as given by

$$S_k = A_k^T S_{k+1} A_k + Q_k - (B_k^T S_{k+1} A_k + P_k^T)^T (B_k^T S_{k+1} B_k + R_k)^{-1} (B_k^T S_{k+1} A_k + P_k^T), \quad (24a)$$

$$\mathbf{s}_k = \mathbf{q}_k + A_k^T \mathbf{s}_{k+1} + A_k^T S_{k+1} \mathbf{g}_k - (B_k^T S_{k+1} A_k + P_k^T)^T (B_k^T S_{k+1} B_k + R_k)^{-1} (B_k^T S_{k+1} \mathbf{g}_k + B_k^T \mathbf{s}_{k+1} + \mathbf{r}_k), \quad (24b)$$

$$c_k = \mathbf{g}_k^T S_{k+1} \mathbf{g}_k + 2\mathbf{s}_{k+1}^T \mathbf{g}_k + c_{k+1} - (B_k^T S_{k+1} \mathbf{g}_k + B_k^T \mathbf{s}_{k+1} + \mathbf{r}_k)^T (B_k^T S_{k+1} B_k + R_k)^{-1} (B_k^T S_{k+1} \mathbf{g}_k + B_k^T \mathbf{s}_{k+1} + \mathbf{r}_k). \quad (24c)$$

Thus, approximately optimal LQR solutions from nonlinear equations of motion about a quadratic cost function can be found which can be used in conjunction with RRT* (Karaman and Frazzoli, 2011) to obtain dynamically feasible continuous trajectories with the asymptotic optimality property. LQR-RRT* consists of seven components including:

- *Random sampling*: The state-space is randomly sampled uniformly to obtain a node (state \mathbf{x}_{rand}).
- *Nearest node*: With \mathbf{x}_{rand} and a current set of nodes \mathbb{N} of the tree (trajectory), the nearest node in the tree relative to \mathbf{x}_{rand} is obtained using the value function in Eq. (23) given by

$$\mathbf{x}_{nearest} = \arg \min_{\mathbf{x}' \in \mathbb{N}} (\mathbf{x}' - \mathbf{x}_{rand})^T S_{rand} (\mathbf{x}' - \mathbf{x}_{rand}) + (\mathbf{x}' - \mathbf{x}_{rand}) \mathbf{s}_{rand} + c_{rand}, \quad (25)$$

where S_{rand} , \mathbf{s}_{rand} , and c_{rand} are computed about the time-step which \mathbf{x}_{rand} occurs.

- *LQR steer*: An LQR trajectory is found between nodes $\mathbf{x}_{nearest}$ and \mathbf{x}_{rand} . Note that the trajectory found can be a path that moves towards \mathbf{x}_{rand} with a final state \mathbf{x}_{new} .
- *Near nodes*: Using \mathbf{x}_{new} and set \mathbb{N} , a subset of nodes $\mathbb{N}_{near} \subseteq \mathbb{N}$ is found within the vicinity of \mathbf{x}_{new} using Eq. (23) given by

$$\left\{ \mathbf{x}' \in \mathbb{N} : (\mathbf{x}' - \mathbf{x}_{new})^T S_{new} (\mathbf{x}' - \mathbf{x}_{new}) + (\mathbf{x}' - \mathbf{x}_{new}) \mathbf{s}_{new} + c_{new} \leq \gamma \left(\frac{\log n}{n} \right)^{1/n_x} \right\}. \quad (26)$$

- *Choosing a parent*: LQR trajectories for each node in \mathbb{N}_{near} are found with respect to \mathbf{x}_{new} . The node with the lowest cost (\mathbf{x}_{min}) and the trajectory σ_{min} becomes the parent node of \mathbf{x}_{new} .
- *Collision checking*: The trajectory σ_{min} is checked against any obstacles within the state-space and is further discussed in the Collision Avoidance subsection.
- *Rewire near nodes*: If σ_{min} and \mathbf{x}_{new} are collision-free, \mathbf{x}_{new} is added to the set of nodes \mathbb{N} , and then attempts are made to reconnect \mathbf{x}_{new} with the set \mathbb{N}_{near} with LQR trajectories if the cost is less than its current parent node.

This algorithm provides a single pass of LQR-RRT* which generates collision-free trajectories built from sampling. Sampling through LQR-RRT* may provide jerky and unnatural paths if not enough samples are taken, thus, trajectory smoothing through LQR shortcutting is applied to reduce this effect and provide collision-free trajectories.

4.1.2 An Alternative Global Planning Module: Kinodynamic RRT

Global planning with considerations for real-time use might also be desirable, particularly if replanning is required. First proposed by (LaValle, 2001), kinodynamic-RRT (kino-RRT) explores the state space rather than configuration space and enjoys the benefits of explicit evaluation of constraints, including dynamics. Essentially, forward evaluation of the dynamics is incorporated into **steer** and an appropriate distance metric is developed so that **nearest** works appropriately. This can be fast enough for online deployment, but can at least provide reference solutions to other solvers that fail from poor initial guesses. Pseudo-code for the algorithm is provided in Fig. 2. An adapted version of Guided-Kino-RRT is considered, proposed in (Albee, 2019) for a low-dimensional satellite system. Section 4.1.3 discusses the motion primitive approach that enables fast planning.

4.1.3 Motion Primitives

The Guided-Kino-RRT algorithm is summarized in Fig. 2, which uses a few modifications for sufficient speed to be usable in real-time. First, a simple cost-to-go distance metric, weighted Euclidean distance to the desired \mathbf{x}_{rand} is used,

$$J = \|\mathbf{x} - \mathbf{x}_{rand}\|_{\mathbf{w}} \quad (27)$$

where \mathbf{w} represents variable weightings on desired values of the state space. While not a true approximation of the cost-to-go, this metric is simple and allows for adjustment of different values of the state space based on relative priority for the system of interest.

Second, progress toward minimizing this metric during **steer** is accomplished by selection of representative motion primitives. Motion primitives are actions $\mathbf{u}(t) : t \in [t_0, t_a]$ where t_a is a specified action length. Motion

```

procedure GUIDED-KINO-RRT( $\mathcal{X}, \mathcal{U}$ )
   $V \leftarrow \mathbf{x}_{init}; E \leftarrow \emptyset;$ 
  while  $\mathbf{x}_{err} > tol$  do
     $\mathbf{x}_{rand} \leftarrow \text{sampleFree}$ 
     $\mathbf{x}_{nearest} \leftarrow \text{nearest}(V, x_{rand})$ 
     $\mathbf{x}_{new} \leftarrow \text{guidedSteer}(\mathbf{x}_{nearest}, \mathbf{x}_{rand})$ 
    if  $\text{ObstacleFree}(\mathbf{x}_{nearest}, \mathbf{x}_{new})$  then
       $V \leftarrow V \cup \mathbf{x}_{new}; E \leftarrow E \cup (\mathbf{x}_{nearest}, \mathbf{x}_{new});$ 
  return  $G = (V, E);$ 

```

Figure 2: Guided-Kino-RRT, used by the replanning-enabled global planning module.

primitives reduce the branching factor of selecting an “optimal” action that makes the closest approach to \mathbf{x}_{rand} ; from the infinite set of possible inputs to apply, only a set of inputs that are “reasonable” are used. There are numerous methods for choosing motion primitives, and they feature in a number of motion planning schemes that consider system dynamics, but a general rule of thumb is that the motion primitives be representative of the typical motions the system might execute. Note that in practice one must use an ordinary differential equation solver to compute $\mathbf{x}(t_a)$ per action—this might require selecting an additional timestep $dt < t_a$ for the integration scheme.

Because the goal of the global planner is mainly to enable efficient collision-checking the translational dynamics are primarily of interest for the free-flyer system (those which most significantly affect obstacle collision), which can be represented by the double integrator dynamics for a space system, or a dynamic Dubins car for a ground vehicle, for instance. A simple motion primitive selection method yields a surprisingly effective balance between sufficient description of the action set and computational burden. For the current constraint set \mathcal{U} , $\forall u_i \in \mathbf{u}$ select $u_i^+ = cu_{i,max}$ and $u_i^- = cu_{i,min}$ where $c \in [0, 1]$. Then, one may assign a motion primitive set \mathcal{U}_{mp} taking the individual application of these min/max sets,

$$\begin{aligned}
 & [u_{i,min}, \dots, \mathbf{0}^\top]^\top, \\
 & [u_{i,max}, \dots, \mathbf{0}^\top]^\top, \\
 & [0, u_{i,min}, \dots, \mathbf{0}^\top]^\top, \\
 & [0, u_{i,max}, \dots, \mathbf{0}^\top]^\top, \\
 & \dots, \\
 & [\mathbf{0}^\top]
 \end{aligned} \tag{28}$$

which will result in an action set of size $2m + 1$, with the addition of the zero “no action” option. c is a scaling option of the max desired motion input which should be chosen conservatively in the event that initial dynamics knowledge is inaccurate, which could invalidate a dynamically feasible plan. Additionally, a t_a must be selected which, again, is most useful to consider in the context of the desired obstacle density with respect to the speed of the dynamics of interest—very small t_a will lead to small `steer` steps and many more node expansions; large t_a might easily expand nodes beyond typical obstacle density distance, or miss the fidelity of shorter applications of input in making connection decisions, Fig. 3. (This is also true for velocity states—tight \mathcal{X} constraints cannot be repeatedly violated or node expansions will be fruitless.) It is emphasized that rough approximations like the above motion primitive selection method above are not an extreme concern because:

- Replanning is anticipated—it is not worth creating a time-intensive, perfectly crafted global plan for a nominal set of dynamics.
- Trajectory optimization is often performed using either a smoothing approach or a local planner—

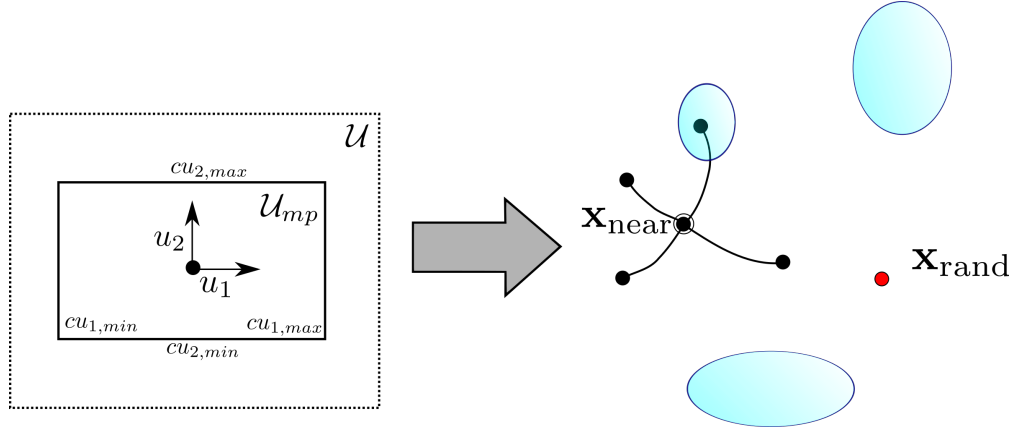


Figure 3: Motion primitives (right) result from the selection \mathcal{U}_{mp} (left). Motion primitives must be carefully selected based on state constraints \mathcal{X} , especially obstacle density (light blue), which will reject unsuccessful expansions.

global plan solutions are effectively guiding initializations with the main goal of enforcing obstacle constraints while remaining dynamically feasible.

4.2 Collision Avoidance

In order to prevent collisions between the free-flyer and e.g., an assembled structure, collision avoidance must be considered to remain in \mathcal{X}_{free} . Utilizing the advantage of a direct collision checking module is one of the most useful benefits of selecting a sampling-based planner; sampling-based motion planners (e.g. RRT*) include a collision checking feature which is used to generate collision-free trajectories between two nodes (states). If the trajectory between two nodes intersects with an obstacle, the trajectory is thrown out, and a new trajectory is generated at the next iteration. The goal for the on-orbit free-flyer is to plan trajectories for structural assembly under inertial uncertainty while avoiding these obstacles. It is assumed that the obstacles themselves are tracked by either the free-flyer or another spacecraft. By knowing the obstacle states through obstacle tracking, the on-orbit free-flyer can approximate keep-out zones.

There are a number of possible obstacle representations—one may use ellipsoidal-on-point constraints for instance in order to perform simple collision checking, which are common for e.g., space robotics motion planning scenarios (Jewison et al., 2015). A more sophisticated method unique to sampling-based planners, ellipsoidal-on-ellipsoidal collision checking is also covered here.

4.2.1 Ellipsoid-on-Point Constraints

Ellipsoidal obstacle collision checking can be performed via

$$(\mathbf{x} - \mathbf{x}_c)^\top \mathbf{P} (\mathbf{x} - \mathbf{x}_c) \geq 1$$

$$\mathbf{P} = \begin{bmatrix} \frac{1}{a^2} & 0 & 0 \\ 0 & \frac{1}{b^2} & 0 \\ 0 & 0 & \frac{1}{c^2} \end{bmatrix}$$

where \mathbf{P} is the ellipsoid shape matrix and a , b , and c are semi-major and semi-minor axis lengths of the ellipsoid centered at \mathbf{x}_c . This is a handy quadratic constraint that can be added on to optimization-based

formulations, or used as a black box collision check for sampling-based planning. However, ensuring safety requires expanding the bounding ellipsoid to be sufficiently large to also include the robot’s own bounding geometry since the check is only whether a point representation of the robotic system is included within the ellipsoid’s volume—this can lead to extremely conservative collision-checking solutions.

This formulation may also be used as a constraint in optimization-based approaches, though it is nonlinear and nonconvex; for sampling-based motion planning, it is a simple check used for generating collision-free segments. Although this work assumes that obstacles are static once they are assembled, dynamic updates to the obstacle state, \mathbf{x}_c , can also be integrated (Albee, 2022). Note, that considerations must be made for ill-posed motion planning problem; if the free-flyer moves with a high velocity, the time update for the position for the discrete system may jump quickly if the time interval is not fine enough. If the distance for two consecutive position states is larger than the smallest characteristic length of the ellipsoid, the algorithm will not detect a collision, although in reality (continuous time), a collision may occur. A simple method to mitigate this problem is to increase the sample resolution time and by interpolating the trajectory during the collision check (Jewison, 2017).

4.2.2 Ellipsoid-on-Ellipsoid Convex Collision Checking

An improved collision-checking module, unusable for optimization-based planners except perhaps with pre-computed signed distance fields, uses any of a number of convex collision checking algorithms (e.g., (Yi-King Choi et al., 2009)) to compute convex-on-convex shape collisions. This allows, for instance, a bounding ellipsoid placed around robot collision geometry to be used without performing obstacle inflation for ellipsoid-on-point checking. Using an ellipsoidal-on-ellipsoidal representation, efficient convex collision checking algorithms may be employed for more precise three-dimensional collision detection; the approach of (Yi-King Choi et al., 2009) is applied for the real-time kino-RRT planner.

4.3 Trajectory Smoothing by LQR Shortcutting

Given the LQR-RRT* or other global trajectory which may contain jerky and unnatural paths, trajectory smoothing can be directly applied using a shortcutting approach which iteratively constructs path segments between existing nodes (Kallmann et al., 2008; Geraerts and Overmars, 2007; Hauser and Ng-Thow-Hing, 2010). This enables the generation of high-quality, collision-free, smooth paths that can be used directly for control. Specifically, LQR shortcutting algorithm is presented which generates dynamically feasible shortcut segments that are optimal to the LQR cost function given by Eqs. (7) and (8).

- *Random sampling*: From the initial trajectory σ_0 , two nodes, \mathbf{x}_a and \mathbf{x}_b , are randomly sampled which results in a trajectory with three sections, $\sigma_0 = [\sigma_1, \sigma_2, \sigma_3]$.
- *LQR Interpolation*: An interpolation using an LQR solution between \mathbf{x}_a and \mathbf{x}_b is determined. The new trajectory is $\sigma_{2,interp}$. This solution incorporates dynamic feasibility and optimality in the generated shortcut.
- *Collision Checking*: Lastly, the new trajectory $\sigma_{2,interp}$ is checked against any obstacles within the state-space which is discussed in the Collision Avoidance subsection. If the shortcut is collision-free, then $\sigma_{2,interp}$ is patched with the two other sections σ_1 and σ_3 into $\sigma_{new} = [\sigma_1, \sigma_{2,interp}, \sigma_3]$.

By applying LQR shortcutting on the LQR-RRT* trajectory, high-quality, collision-free, smooth paths that are dynamically feasible for the on-orbit free-flyer is generated. Thus, control can be applied to track this trajectory.

4.4 Information-Aware Motion Planning and Parameter Estimation

Also known as active learning, the goal of information-aware planning is to enable the agent to actively explore the environment in order to improve accuracy and efficiency of the learning procedure. In an on-orbit assembly context, this would be useful when interacting with new payloads that may not be fully inertially characterized. In the case of parametric system identification procedures, information-aware planning occurs in the form of excitation trajectories found through constrained nonlinear optimization of metrics based on sensor information, called optimality criteria, e.g. the condition number (the ratio between the largest and smallest singular values of the input correlation matrix) (Armstrong, 1989). Some other criteria are based on the Fisher Information Matrix (FIM), which is a measure of the amount of information provided by the measurements about the unknown parameters. Considering $\boldsymbol{\theta}$ as the vector of parameters of interest, and $\tilde{\mathbf{y}}$ as the measurements, the FIM is calculated as

$$\mathbf{F} = \mathbb{E} \left[\left[\frac{\partial}{\partial \boldsymbol{\theta}} \ln [p(\tilde{\mathbf{y}}|\boldsymbol{\theta})] \right] \left[\frac{\partial}{\partial \boldsymbol{\theta}} \ln [p(\tilde{\mathbf{y}}|\boldsymbol{\theta})] \right]^T \right]. \quad (29)$$

If the information content in the measurement data is maximized, then it would also correspond to minimizing the lower bound on the variance of the estimates (Crassidis and Junkins, 2004). Optimization of the FIM is therefore a good candidate for design of information-rich trajectories. Measures of identifiability based on the information matrix, referred to as the alphabet optimalities (Siciliano and Khatib, 2016) include A optimality, which maximises the trace of the inverse FIM, or E optimality, where the least eigen value of the FIM is maximized. Following previous research works by the authors (Albee et al., 2019; Ekal et al., 2021), the A -optimality criterion is used for generating local information-aware motion plans in this work.

For the on-orbit assembly scenario in question, performing a complete system identification procedure for each assembly component to be transported could be a redundant procedure at the expense of energy and time. Rather, the goal is to obtain a sufficient amount of uncertainty reduction post grasping, as the robot transports the component to the assembly location. This information, if taken into account, will enable more precise and optimal task execution without being overly cautious. The following discretized trajectory optimization problem is solved for obtaining on-the-fly adjustable information incentivization:

$$\begin{aligned} \underset{\mathbf{u}}{\text{minimize}} \quad & J = \sum_{k=0}^{N-1} \mathbf{x}_{t+k}^\top \mathbf{Q} \mathbf{x}_{t+k} + \mathbf{u}_{t+k}^\top \mathbf{R} \mathbf{u}_{t+k} + \boldsymbol{\Gamma}^\top \text{diag}(\mathbf{F}^{-1}) \\ \text{subject to} \quad & \mathbf{x}_{t+k+1} = f(\mathbf{x}_{t+k}, \mathbf{u}_{t+k}, \boldsymbol{\theta}), k = 0, \dots, N-1 \\ & \mathbf{x}_{t+k} \in \mathcal{X}_{free}, k = 0, \dots, N, \\ & \mathbf{u}_{t+k} \in \mathcal{U}, k = 0, \dots, N-1, \end{aligned} \quad (30)$$

where N is the horizon length and $\mathbf{Q} \succ 0$ and $\mathbf{R} \succ 0$ are weighting matrices. The relative weighting term, $\boldsymbol{\Gamma} \in \mathbb{R}^j$, is used to tune the amount of information content of the trajectory. The output $\mathcal{P}_l := \{\mathbf{x}_{t:t+N}, \mathbf{u}_{t:t+N-1}\}$ is made available for control over horizon N .

The evolution of $\boldsymbol{\Gamma}(t)$ can be designed based on dynamical and environmental considerations. A decline and eventual shut-off in the information gain content as the robot reaches the goal position, $\boldsymbol{\Gamma}$ can be modeled on heuristics like the decreasing exponential. This work employs a decay method guided by the current covariance of the estimates (Albee et al., 2022), leading to $\boldsymbol{\Gamma}$ being zero once the current model characterization is within a desired precision tolerance. Selective information content can be assigned by tweaking weightings individually per parameter. In other words, at local plan horizon starting at t_{k+1} , for all parameters of interest i with variance $\sigma_{i,k}$, desired learning tolerance σ_n, i , the value of relative weighting per parameter, γ_i , is determined as shown in Fig. 4. α and β are tuning parameters.

```

1: procedure COVARWEIGHT( $\Sigma_n, \Gamma_0, \alpha, \beta$ )
2:    $\Sigma_{k+1} \leftarrow \text{UpdateCovar}(\Sigma_k)$ 
3:   for  $\forall i$  do
4:     if  $\sigma_i \leq \alpha \sigma_{n,i}$  then
5:        $\gamma_i \leftarrow 0$ 
6:     else
7:        $\gamma_i \leftarrow \gamma_{i,0} \exp^{-\frac{\beta \sigma_{n,i}}{\sigma_i}}$ 

```

Figure 4: The covariance-based information weighting procedure to determine parameter weightings can be automatically adjusted to within a learning tolerance.

4.4.1 Sequential Parameter Estimation

Considering that tracking current model knowledge is of interest, a rapid and sequential method of estimation, such as recursive least squares is used for inertial parameter estimation. The estimation problem can be formulated as

$$\tilde{y} = \mathbf{H}\theta + v, \quad v \sim N(0, \mathbf{W}) \quad (31)$$

Where $\theta = [1/m \ 1/I_{xx} \ 1/I_{yy} \ 1/I_{zz}]^T$ are the mass and moments of inertia parameters respectively. \tilde{y} represent the measurement data, in this case linear acceleration, \mathbf{a} and angular acceleration, $\boldsymbol{\alpha}$ (obtained from differentiation of angular velocities). Representing the control inputs as $\mathbf{F} \in \mathbb{R}^3$ (forces) and $\boldsymbol{\tau} \in \mathbb{R}^3$ (torques), the regressor matrix \mathbf{H} can be written as

$$\mathbf{H} = \begin{bmatrix} \mathbf{F} & \mathbf{0}_{3 \times 3} \\ \mathbf{0}_{3 \times 1} & \boldsymbol{\tau} \mathbf{I}_{3 \times 3} \end{bmatrix} \quad (32)$$

Resembling the update step of the Kalman filter without a process model, the recursive least squares algorithm at every time step is given as (Crassidis and Junkins, 2004)

$$\begin{aligned} \theta_{k+1} &= \theta_k + \mathbf{K}_k(\tilde{y}_k - \mathbf{H}_k \theta_k) \\ \mathbf{P}_{k+1} &= (\mathbf{I} - \mathbf{K}_k \mathbf{H}_k) \mathbf{P}_k \end{aligned}$$

where

$$\mathbf{K}_k = \mathbf{P}_k \mathbf{H}_k' (\mathbf{H}_k \mathbf{P}_k \mathbf{H}_k' + \mathbf{W})^{-1}$$

Details on outlier rejection and accounting for latency are discussed in 6.2.1.

4.5 Robust Model Predictive Control

A control framework is sought which is flexible in its modeling capability, capable of handling real-time computation, and ideally containing robustness guarantees against unstructured uncertainties, $\mathbf{w}_x \in \mathbb{W}$. Robust tube model predictive control fits these criteria, making it an appropriate choice for trajectory tracking of local plan output, requiring a few ingredients: a reference trajectory $\mathbf{x}_{ref}(i)$, a reference input $\mathbf{u}_{ref}(i)$, a dynamics model \mathcal{M} , and a predicted bound on disturbances to the discrete-time dynamics to form robustness guarantees. \mathbf{w}_x supplies the uncertainty, and is often conveniently modeled as a set of box constraints,

$$\mathbb{W} = \left\{ \mathbf{w} \in \mathbb{R}^n : \begin{bmatrix} \mathbf{I}_6 \\ -\mathbf{I}_6 \end{bmatrix} \mathbf{w} \leq \begin{bmatrix} \mathbf{I} \mathbf{w}_{max} \\ \mathbf{I} \mathbf{w}_{max} \end{bmatrix} \right\}. \quad (33)$$

For the linear case (e.g., translational dynamics), the free-flyer error dynamics are then

$$\mathbf{x}^+_{err} = \mathbf{A}\mathbf{x}_{err} + \mathbf{B}\mathbf{u}_{err} + \mathbf{w}_x. \quad (34)$$

where $\mathbf{x}_{err} = \mathbf{x} - \mathbf{x}_{ref,i}$ and $\mathbf{u}_{err} = \mathbf{u} - \mathbf{u}_{ref,i}$. \mathbf{w}_x can be thought of as a combination of any unstructured noise uncertainty, as well as any uncertainty due to imperfect system modeling (e.g., incorrect parameter estimates, $\hat{\boldsymbol{\theta}}$).

The stochastic dynamics are now in a suitable format for linear robust tube MPC. First, a disturbance rejection controller called the ancillary controller must be used to reject disturbance from a nominal MPC trajectory. The ancillary controller takes the form below, and is added onto a nominal MPC input, \mathbf{v} :

$$\mathbf{u}_{anc} = \mathbf{K}_{anc}(\mathbf{x} - \bar{\mathbf{z}}) \quad (35)$$

$$\mathbf{u} = \mathbf{v} + \mathbf{u}_{anc} \quad (36)$$

where \mathbf{v} is a nominal actuation determined by a deterministic MPC and \mathbf{K}_{anc} indicates the ancillary controller disturbance rejection gain, and $\bar{\mathbf{z}}$ is a nominal state not necessarily the same as the real initial state. \mathbf{K}_{anc} can be determined through a simple LQR procedure on the nominal dynamics, but provides optimal performance and better robustness guarantees when determined via a tube minimization procedure (Buckner and Lampariello, 2018). That is, if the robust positively invariant set (RPI) can be minimized through the choice of \mathbf{K}_{anc} then more rigorous guarantees exist; namely, the tube robustness guarantee that if the system state \mathbf{x} starts within a set \mathbb{Z} centered around a planned control trajectory \mathbf{z} , under the given uncertainty and ancillary controller it will remain with a tube around this trajectory for all possible \mathbf{w}_x disturbances. The tube robustness guarantee can be thought of simply as “if you start in the tube, you stay in the tube.”

Secondarily, the actual nominal MPC trajectory \mathbf{z} used by the ancillary controller must be determined. The error dynamics of Equation 34 are used. \mathbb{U} and \mathbb{X} are converted to tightened constraints, effectively giving up control authority to the ancillary controller for disturbance rejection. These tightened constraints are indicated as $\mathbf{x} \in \bar{\mathbb{X}} \subset \mathbb{X}$ and $\mathbf{u} \in \bar{\mathbb{U}} \subset \mathbb{U}$ and are derived from the nominal box constraints, \mathbb{X} and \mathbb{U} . The exact constraint tightening procedure can be found in both Buckner and Limon (Buckner and Lampariello, 2018) (Limon et al., 2008). A notable feature observed in this constraint tightening procedure is the fact that large uncertainty bounds will make constraint tightening infeasible. This serves as a notification that the considered uncertainty levels are beyond the system’s actuation and/or dynamics capability to adequately counter. It is possible to compromise and settle for a lower level of robustness with a lower assumed \mathbf{w}_x or to even require replanning at prior stages of the pipeline. Finally, the nominal MPC (which does not necessarily align with the initial real state, \mathbf{x}_i) can be found by solving

$$\min_{\mathbf{u}^{(i)}, \bar{\mathbf{z}}_0} J = \sum_{i=0}^{N-1} [\bar{\mathbf{z}}_i - \mathbf{x}_{i,ref}]^\top \mathbf{Q} [\bar{\mathbf{z}}_i - \mathbf{x}_{i,ref}] + [\bar{\mathbf{v}}_i - \mathbf{u}_{i,ref}]^\top \mathbf{R} [\bar{\mathbf{v}}_i - \mathbf{u}_{i,ref}] +$$

$$[\bar{\mathbf{z}}(N) - \mathbf{x}_{ref}(N)]^\top \mathbf{H} [\bar{\mathbf{z}}(N) - \mathbf{x}_{des}(N)]$$

subject to

$$\mathbf{z}_i^+ = f(\mathbf{z}_i, \mathbf{v}_i),$$

$$\bar{\mathbf{z}} \in \bar{\mathbb{X}}$$

$$\bar{\mathbf{v}} \in \bar{\mathbb{U}}$$

$$\bar{\mathbf{v}} \in \mathbf{x} \bigoplus (-\mathbb{Z}).$$

Equation 36 is executed for the first timestep of the nominal MPC solution until the solution can be recomputed at i^+ .

A key observation explored in recent work by Albee and Ekal (Albee et al., 2022) is that reachable sets can sometimes be updated in real-time based on available data. Re-computation of \mathbb{Z} , then, might allow one to ease off of overly conservative robustness guarantees based on the latest available system data (e.g., learned inertial parameters).

4.6 Approach: Planning, Control, and Estimation Techniques for Free-Flyer On-Orbit Assembly

These planning and control components can be assembled in two primary modes of operation: (1) offline, pre-motion computation and (2) online, real-time computation. Offline computation provides benefits in terms of additional time to refine global plan solutions, create robustness guarantees, and other computationally-intensive operations. Offline computation might be desirable if on-orbit operations will permit additional time in creating motion plans, if model certainty is high, or if refined motion plans are highly desirable. Meanwhile, online computation is desirable if models or environmental constraints are unknown or changing, or if additional computation time is unacceptable for the operation of interest. At the cost of producing solutions that might be less optimal, online computation allows adaptation to changing conditions and replanning capability.

These offline and online computation methods are combined in a sample on-orbit assembly scenario, which consists of three types of maneuvers:

1. Offline planning that can be produced in passive waiting areas. System model knowledge is considered adequate and robust tracking is unnecessary.
2. Online planning, control, and estimation that is responsive to poor model knowledge and has a time sensitivity—real-time plans are desirable.
3. Offline planning that can be produced in passive waiting areas. System model knowledge is considered adequate, but there is uncertainty that makes robust tracking desirable.

These maneuvers are demonstrated between three waypoints, (a), (b), and (c). These waypoints represent an assembly “construction site area”, a “storage area” and a “safe area,” respectively and are illustrated in Fig. 5. At waypoint (b), the storage area, the free-flyer acquires new payload to transport, modifying its model inertial parameters, θ . The (a)-(b) maneuver is an offline plan without robust tracking; the (b)-(c) maneuver uses the RATTLE algorithm to perform model improvement post payload capture; and the (c)-(a) maneuver is an offline plan with robust tracking. Combined, these maneuvers represent typical situations that a free-flyer manipulating payload might find itself in, with respect to the safety of its current surroundings, the quality of its model knowledge, and the time urgency of progressing toward its goal. All maneuvering takes into account a central obstacle constraint (posed as ellipsoid-on-point for LQR-RRT* and ellipsoid-on-ellipsoid for kino-RRT).

Table 1: Planning and control elements for each portion of the on-orbit assembly sequence. Components indicated are for the maneuver immediately following the listed waypoint.

Waypoints	Designation	Online Planning	Robust Tracking	Model Improvement
A-B	Construction Site	✗	✗	✗
B-C	Storage Area	✓	✓	✓
C-A	Safe Area	✗	✓	✗

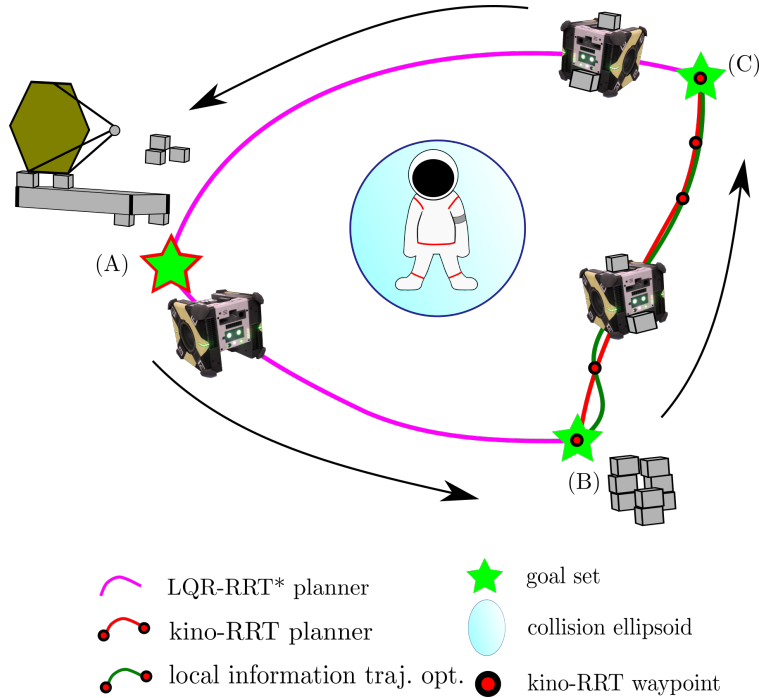


Figure 5: The on-orbit assembly sequence, combining elements of online and offline planning, robust control, and model improvement.

5 Implementation, Environment, and Operational Details

The on-orbit assembly modules of Section 4 were implemented to run alongside the Astrobees Flight Software for the Astrobees robots (Bualat et al., 2015; Smith et al., 2016a) aboard the International Space Station (ISS). The Astrobees robots, shown in Fig. 6, are cube-shaped 30 cm wide reprogrammable robots on the ISS that have been reconfigured by the ReSWARM experiments for autonomy and controls research (Albee et al., 2020). This section overviews some of Astrobees key software and environmental details, as well as some of the unique obstacles that arose in configuring the robots for on-orbit assembly experimental testing.

5.1 Key Software Information

The Astrobees Robot Software uses ROS as middleware for communication, with about 46 nodelets grouped into approximately 14 processes running on two ARM processors (Flückiger et al., 2018) (with one additional Android-based High-Level Processor). The Astrobees Robot Software also includes a high-fidelity simulator, which enables testing of developed algorithms before implementation on hardware; in simulation, a single local computer simulates running all nodes/nodelets as if both of Astrobees main processors are available. The physics simulator is essentially a set of plug-ins for the Gazebo robot physics simulator, and offer the same ROS interfaces for sensor communications as the hardware. The ROS/Gazebo-based simulation environment includes extensive modeling of Astrobees including its impeller propulsion system, onboard visual navigation, environmental disturbances, and other true-to-life models (Flückiger et al., 2018).

Astrobees default flight software (FSW) consists of planning (Planner), mapping (Mapper), localization (EKF, N.B.: the localization system is actually factor graph-based), control (CTL), and force application (FAM, i.e., mixer) modules. Uniting these components is a managing node, the choreographer. These elements are shown in Fig. 11. These key autonomy interfaces are overviewed.



Figure 6: The Astrobee robots operating aboard the ISS. (Credit: NASA)

5.1.1 Localization

Astrobee’s localization takes in measurements from various sensors, $\tilde{\mathbf{y}}$ and fuses these together in conjunction with a measurement and dynamics model $h(\mathbf{x}(t))$ and $f(\mathbf{x}, \mathbf{u})$ to produce a state estimate $\hat{\mathbf{x}}$. The measurement model might be very complex or impossible to model in the case of vision-based estimation systems, for example. In these cases, sophisticated algorithms produce pose/state estimate information which is fused alongside other sensor information, like IMU data. Astrobee, for example, has three main measurement sources:

- Visual-inertial odometry (VIO)
- Sparse mapping
- IMU data

Errors in any one of these measurement sources could imperil the state estimation algorithm. For Astrobee, the IMU is particularly noisy, VIO is sensitive to fast attitude movements (motion blur), and sparse mapping relies on an accurate, recent map with clear visual features. (A common issue depending on the recency of mapping activities is the quality and accuracy of the map, which might be distorted and out-of-date.⁴)

Astrobee’s localization system was overhauled in early 2021 to use a new graph-based system utilizing GTSAM, named AstroLoc (Soussan et al., 2022). AstroLoc has higher accuracy than filtering-based methods, is fast enough for real-time use, and handles chirality issues. It is heavily VIO-reliant since landmarks frequently change (i.e., camera image changes are carefully analyzed to estimate motion, combined with IMU info). The latest iteration of the localization system runs at about 5 [Hz], though updates upsample to a rate of 62.5 [Hz] (half the IMU update rate).

⁴There are a few methods to determine if localization data is accurate in the absence of ground truth:

- Get ground truth—sometimes sources like video footage can give clues if localization is obviously inaccurate.
- Check for physically infeasible changes in state. Compare estimates against the largest deviations possible given the system dynamics. (This might also be used as a check to reject bad estimates.)
- Look at estimation signs of health, like feature counts, that show if measurements might be troubled.
- Check for small-scale “jumpiness” that might lead to controller problems.

5.1.2 Controller

The controller, receives $\hat{\mathbf{x}}$ from the localization system. The controller then takes a desired trajectory \mathbf{x}_{des} and tuning parameters, ultimately producing a requested input, \mathbf{u} . By default, Astrobee uses a PD controller for the attitude and position controller running at 62.5 [Hz]. Astrobee’s controller does not account for input saturations.

5.1.3 Mixer

Astrobee has a holonomic thruster placement, with 12 independent thrust vents. It generates thrust by drawing in air through two central impellers and expelling it through the vents. The mixer takes requested inputs \mathbf{u} and maps these to permissible actuator commands, i.e., vent opening angles. A thruster placement diagram and explanation is given in (Smith et al., 2016b). The physical properties of the impeller and the nozzles, such as the nozzles’ minimum/maximum open angles, etc. can be found in (Albee et al., 2020), from which the mixer can be determined. For Astrobee, the mixer is not as simple as the typical matrix found in impulsive systems like the SPHERES robots (Jewison, 2014). Actual forces and torques applied may be significantly different from those requested by the control if the control is physically infeasible (i.e., does not satisfy \mathcal{U}), leading to control input saturation.

5.2 Environments

The Astrobee simulation environment includes both the granite world for simulating 3DoF, planar ground testing, and the space station environment for simulating full 6DoF testing. Testing in simulation and multiple subsequent ground-test opportunities enabled ReSWARM’s transition to hardware and the evaluation of its performance on real resource-constrained processors leading up to microgravity testing.

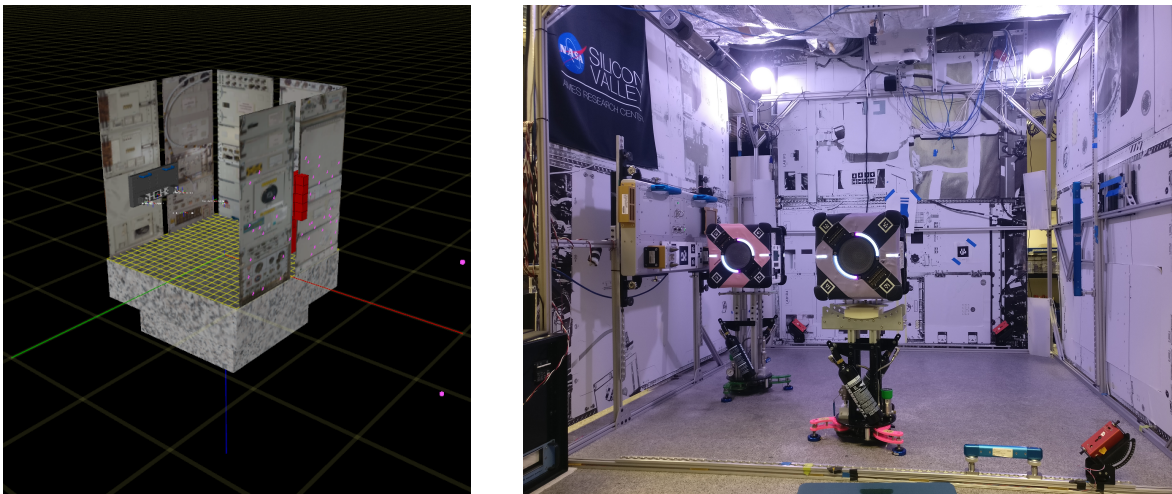


Figure 7: Astrobee’s simulation and physical granite environment. (L) The coordinate convention for granite world. RGB corresponds to XYZ for the axes shown, where z+ points down. (R) The granite table ground facility at NASA Ames, with Bsharp and Wannabee shown.

5.2.1 Ground (Granite) Environment

The granite world in simulation mimics the granite table in use at the NASA Ames ground test facility, where the robots are placed on air-bearing surrounded by a mock-up of the interior of the space station. The simulation table is 2×2 [m]. The coordinate system mimics that of the ISS, where z+ is toward GND (down). The simulation and physical ground facility is shown in Fig. 7.

5.2.2 ISS Environment

The ISS simulation world is a mockup of the US Orbital Segment of the International Space Station, shown in Fig 8. Like in the ISS facility, Astrobee is docked in the Japanese Experiment Module (JEM) of this segment and operates primarily within that module. The approximate volume of this segment is $1.5 \times 6.4 \times 1.7$ [m], in ISS coordinates. The coordinate system and simulation environment (with JEM in the upper left) is shown in Fig. 8. The actual ISS facility is shown in Fig. 9.

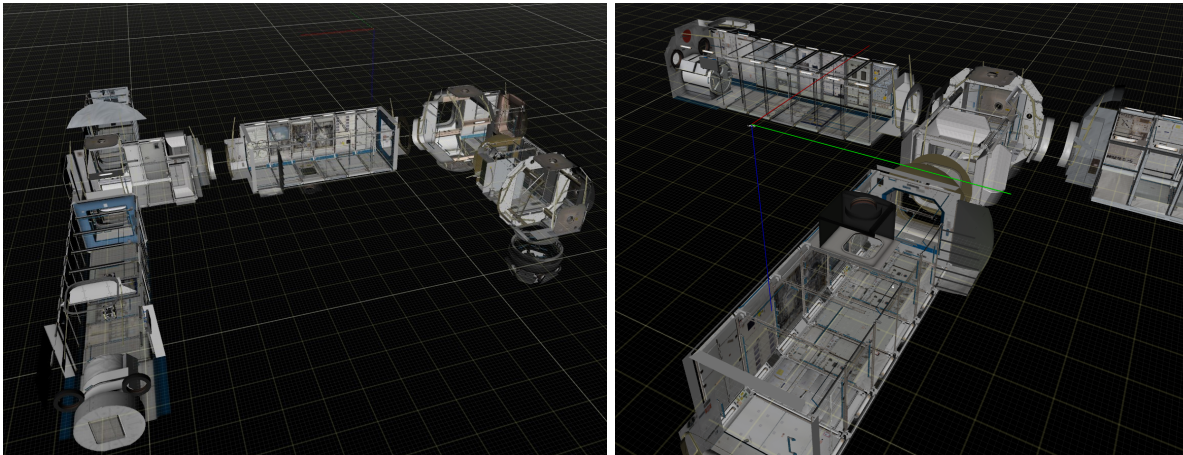


Figure 8: The US segment of the International Space Station, within which Astrobee is permitted to operate. At right, RGB corresponds to XYZ for the axes shown.



Figure 9: The JEM on the ISS which serves as the on-orbit test facility. Astrobee Bumble is shown at center. This particular view is looking PORT (in the +y-axis direction).

5.3 Actuation and motion constraints

Astrobee’s default FSW uses PID control, and its choreographer module broadcasts information about certain keep-out zones for one of the two available planners to use. Therefore, reasoning about actuation and motion constraints to be incorporated in ReSWARMS’s optimization-based planning and control frameworks was essential to ensure feasible and safe trajectory generation and execution in micro-gravity.

5.3.1 Force and torque constraints

The quoted maximum thrusts per axis at various impeller fan speeds are given in Table 2. Vents on the x-axis have the largest nozzles and thus have the maximum acceleration capability, as the table shows. These maximum force values are approximate based on empirical data produced by NASA Ames. Astrobee’s thruster offset is about 0.1 m from the center of mass, so the torque limit is very roughly about $\frac{1}{10}$ of each of these values.

Table 2: The approximate thruster maximum forces per axis.

Motor Speed [RPM]	x-axis [N]	y-axis [N]	z-axis [N]
2000 RPM	0.452	0.216	0.257
2500 RPM	0.680	0.332	0.394
2800 RPM	0.849	0.406	0.486

To mitigate the reduction in localization accuracy due to loss of features, the motion planning algorithm used more conservative limits than those presented in Table 2.

5.3.2 Position and Velocity Constraints

Astrobee has a number of keep-out zones defining rough exterior boundaries of the enclosing environment. Position constraints are not necessarily enforced by any default Astrobee planner or controller (one planner, `planner_qp`, see Fig. 11, does obey keep-in/keep-out zones, but not all of them.). In practice, position constraints must be estimated based on actual setup conditions, especially so for the ISS. On ISS, cargo and objects are regularly reconfigured. The authors have found the following constraints (in metres) to be a good “safe” approximation of the JEM interior volume, in coordinates relative to the approximate JEM centroid located at (10.9, −6.65, 4.9),

$$\begin{aligned} -0.65 &\leq x \leq 0.65 \\ -3.2 &\leq y \leq 3.2 \\ -0.8 &\leq z \leq -0.8. \end{aligned} \tag{37}$$

Approximate keep-in zones are shown in Fig. 10. By default, Astrobee uses a $\pm 0.1 \left[\frac{\text{m}}{\text{s}} \right]$ velocity constraint for safety reasons.

5.4 Special Considerations for Hardware Deployment

In addition to algorithmic details, some implementation novelties were required for the successful use of the on-orbit assembly modules within the Astrobee software stack, showing some of the important considerations when moving to hardware.

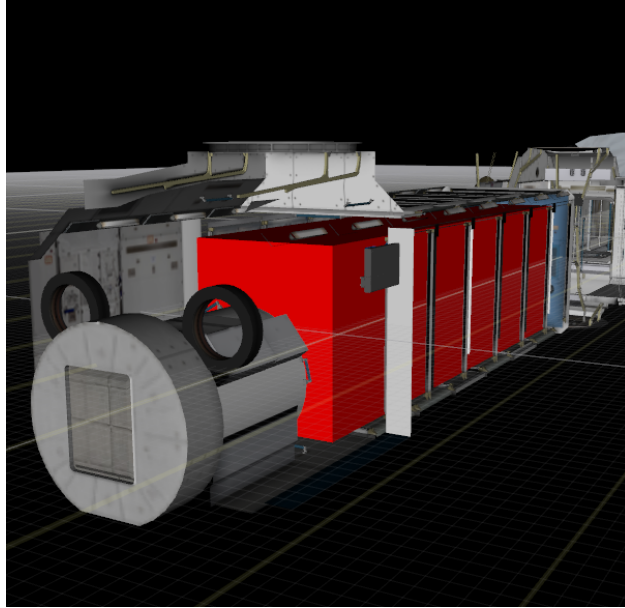


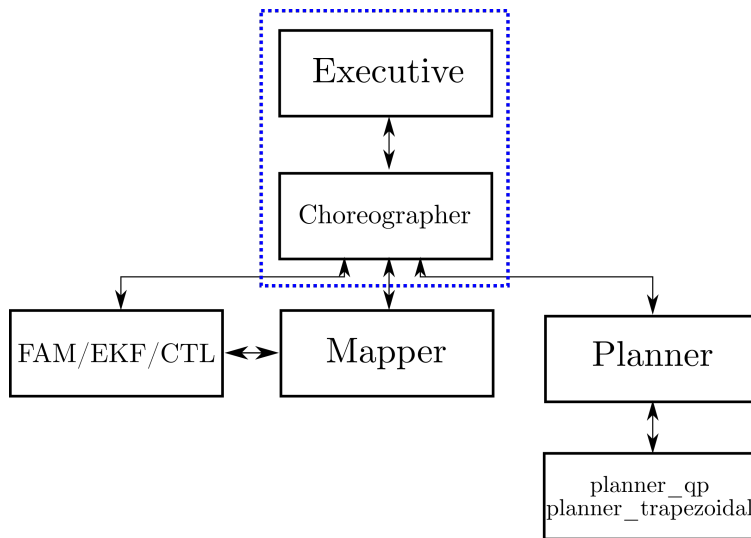
Figure 10: The approximate usable volume of the JEM, in red.

5.4.1 Software Architecture and Complexity

The middleware coordination of the on-orbit assembly modules is non-trivial, and deserves careful consideration to ensure model updates, planner outputs, and other components are on-time and properly shared. On hardware, this role is actually a software package unto itself. While the low-level details of implementing this coordination are not covered here, it is important to ensure that all modules are working from the same set of data and are receiving updates (such as model or constraint updates) at the same time.

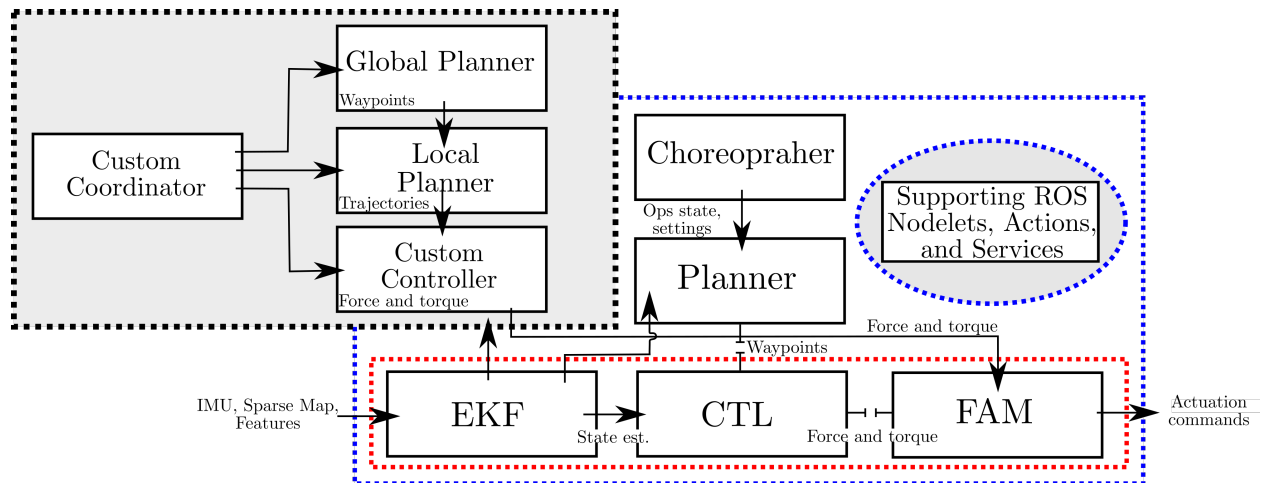
Getting code onto the Astrobee hardware in a safe and reliable way was one of the chief concerns of algorithm integration. Astrobee’s default flight software (FSW) consists of planning (Planner), mapping (Mapper), factor-graph based localizer (EKF), control (CTL), and force application (FAM) modules. Uniting these components is a managing node, the choreographer. These elements are shown in Fig. 11. The components of Astrobee’s default software stack needed to be overridden to run custom autonomy modules. For instance, the modules need to replace default flight software components called EKF, CTL, Planner, and Coordinator. This is possible by adding entirely new nodes that publish ROS messages on the same topics that low-level control elements (FAM) might expect and taking care not to trigger the default software stack. This is important because the default software stack can be left entirely untouched and additional nodes may be added as extra packages on top of existing flight software packages. This greatly simplifies integration and verification. An example of this process is shown in Fig. 12. Additionally, standardization such as working from a single operating system, development environment, and middleware framework (ROS) helps tremendously with this task.

Multiple external libraries, integrated within the Astrobee flight software stack, were used for on-orbit integration. The ACADO toolkit (Houska et al., 2011) was used for solving nonlinear programming of the local planner for parameter learning, and CasADi (Andersson et al., 2019) for implementation of a robust tube MPC. Additionally, Bullet Physics’ C++ collision checker (Coumans,) and Autograd were used for collision detection and additional automatic differentiation, respectively. Cross-compilation of these libraries proved a significant challenge for hardware integration and should be carefully noted when moving to hardware deployment. Highlights of the Astrobee software stack and other implementation hurdles are discussed further in (Albee et al., 2020).



■ Astrobees Flight Software Coordinators

Figure 11: A high-level overview of the relationship of some the Astrobees FSW's default autonomy modules.



■ GNC Subsystem (MATLAB to ROS/C++)

■ Astrobees Flight Software (ROS/C++)

■ Replacement Planning Module (MATLAB/ROS/C++/Python)

Figure 12: An override of the default flight software, using a custom planning and control pipeline. The one sketched here in gray is a rough approximatin of the additional nodes used for ReSWARM testing.

5.4.2 Importance of Localization

Astrobee’s default localization system is under active development, and requires special care in map-building and motion constraints to avoid severe pose estimate jumps, a major challenge for control and inertia estimation. This caused issues for experiments using RATTLE that encouraged rotational motion - in particular information-seeking motion for inertia estimation - sometimes causing significant “jumps” in localization estimates. Localization is the building block of the rest of the autonomy stack, and so localization issues are troubling for all other components. In some cases, this might be viewed as an additional aleatoric disturbance source on the system dynamics.

5.4.3 Timing Considerations, Planning Rates

The various modules run at different rates to accommodate processor capabilities; in addition, elements of Astrobee’s default flight software have their own rates, quirks, and computational loads. Getting the timing right for the various online components of an autonomous system like Astrobee is key for successful operation (especially when the software middleware does not have any real-time guarantees and is simply best-effort—real-time in the sense of a real-time operating system). For instance, Astrobee reports its applied forces and torques (wrench) after passing through the mixer at approximately 62.5 [Hz]. However, this rate can decrease based on processor load. Additionally, reported wrenches are often out-of-order, requiring careful chronological reordering to enable parameter estimation. This is discussed further in Section 6.2.1.

A simple version of the problem is demonstrated in Fig. 13. At left, the global and local plan have different trajectory frequencies, as expected. The global plan waypoints, which might be selected from a higher-fidelity global plan, should coincide with the fixed local planner horizon, which operates over an $N_l * t_l$ length time horizon. It is possible to use differing rates for both planners, but then interpolation will be required. At right, the localization output and reported input do not match up at all, and one data stream might even have variable rates. Again, computations involving the discrete dynamics rely on syncing up function inputs at the same time—a propagation of the model dynamics for an input one second too late could be catastrophic, for instance. In this case, one would need to decide what discretization time to use for the system models, and again might rely on some form of interpolation scheme (or use variable-length integration of the continuous dynamics) to achieve desired results for e.g., the parameter estimation module.

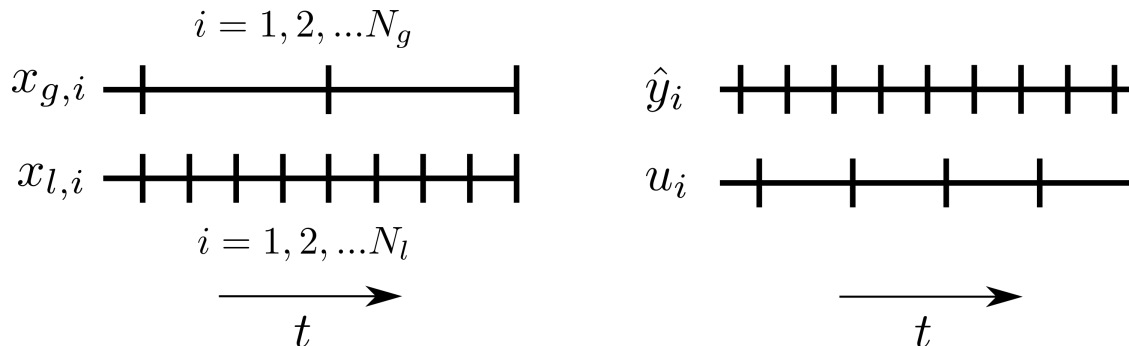


Figure 13: Syncing rates for planning, estimation, and other modules is very important to avoid getting inaccurate data.

If interpolation is required, special care must be taken for interpolation in non-Euclidean manifolds. The quaternions, \mathcal{H} , exist in $\mathcal{SO}(3)$. Simple linear interpolation of Euler angles yields very poor approximations of interpolation along the the 4D unit sphere. Two relatively simple methods provide good quaternion linear and great circle interpolation: LERP and SLERP. SLERP results in manifold-accurate interpolation, with constant angular velocity.

Finally, the frequencies at which the global planner, local planner and, controller and other components

may run at are limited by length of the computation time required on the hardware of the desired robot. Balancing computational burden to obtain sufficient speed on hardware is critical. ISS hardware rates are provided later, in Table 4.

During the extensive ground testing, the computational speeds for the RRT* planners, local planners, MPC horizons, and rate of actuation commands were extensively fine-tuned to ensure real-time operation and planning on desired 6 DOF motion and rates of the Astrobees robots. The overall goal for each Astrobee test was to have each run last less than 5 minutes for the most complex scenario, to maximize extremely precious on-orbit test time. It was also internally noted by previous Astrobee experiments prior to ReSWARM that the ISS Astrobees had more running processes in the background compared to the ground Astrobees. Thus, it was expected that the computational speeds for planning and control were to decrease moving from the ground hardware to the ISS hardware. In consideration of this knowledge, the sample rate for e.g., control was set to 5 [Hz], and the controller defined was adjusted to this rate accordingly to reduce the time complexity of the planning problem and meet the performance requirement.

5.5 Special Considerations for Operations

On-orbit ReSWARM operations required special considerations for preflight, flight, and postflight procedures to mitigate any anomalies during the mission. Field testing using the Astrobee robots is extremely precious time, and therefore preparation and rehearsal for flight activities was key. Some of this special planning is noted here.

5.5.1 Preflight

Preflight operations were performed at the NASA Ames' granite table facility and the Astrobee flight software was used for software integration. Ames' stellar operations staff accommodated ground testing (including many remote test sessions), assisted with software questions, and generally collaborated to improve the Astrobee software experience. Preflight integration occurred in two major ways:

1. The simulation work was integrated with the Astrobee flight software using the ROS/Gazebo environment. The team developed a number of interfaces to enable the on-orbit testing using Astrobee's default flight software (Albee et al., 2020).
2. The Astrobee flight software was integrated with the hardware and tested at the Ames granite table facility. Integration was performed over many day-long ground test sessions for algorithm improvements and hardware bug fixing. Ames personnel assisted with much of the in-person testing.

5.5.2 Flight

Flight operations were conducted over a months-long process of developing ground and crew procedures to ensure rehearsed readiness for operations day. The crew procedure provides instructions of how ISS crew members should aid in experimentation which follows the general format summarized below:

1. Crew member sets up Astrobee(s) in their home position.
2. Astrobee(s) hold their position, and crew member releases the Astrobee(s) and moves to a waiting area out of the field of view (FOV).
3. Astrobee(s) begin execution of a set of maneuvers designed to demonstrate an aspect of the algorithms of interest.
4. Test concludes, or it is stopped early by the ground operator.

5. Crew grabs Astrobee(s), and a new test is selected. Repeat the procedure for additional tests.

Additionally, operations required several roles to make the sessions run smoothly. Operations personnel adhered to the ground procedures which provided instructions on setting-up the Astrobees, setting up the Ground Data System (GDS), running the tests, troubleshooting the Astrobees, and wrapping-up the session. The roles required for operations are summarized below.

- CLI OP: The person sending command-line commands to the robots, responsible for real-time debugging, and applying workarounds.
- GDS OP: The person sending GDS commands to the robot and responsible for nominal test commanding.
- POIC: The person communicating on S/G with the crew and responsible for communicating intentions to CREW.
- CREW: The crew member assisting with experiments and responsible for setting up and monitoring tests.
- MIT: The ground crew at MIT.
- AMES: The ground crew at NASA Ames.

ISS operations were conducted with the help of a single crew member, whose role was to observe experiments and place two Astrobee robots at their respective start positions at the onset of testing. For ReSWARM-1 and ReSWARM-2, Astronauts K. Megan McArthur and Matthias Maurer assisted in the respective Astrobee sessions. Experiments were conducted in a set of short (2-5 minute) tests that demonstrated various aspects of algorithm of interest. Astronauts required a crew procedure ahead of the test session in order for the session's planning to be clearly communicated in a single checklist-type summary document.

For ReSWARM-1, MIT and AMES worked together remotely in which MIT commanded the GDS OP and CLI OP roles while AMES commanded the POIC role. For ReSWARM-2, MIT and AMES worked onsite together at NASA Ames with MIT commanding the GDS OP and CLI OP roles.

A major flight challenge was the performance of the Astrobee's default localization. Astrobee's localization relies on identifying features within a known map of the ISS, which is a challenging task for a constantly-changing interior. For ReSWARM, tests were designed that minimized rotational motion and pointed toward feature-rich areas to assist in localization performance. When Astrobees were in an initial feature-poor area, crew were provided guidance (following procedure protocol) to initially move Astrobee to feature-rich areas and back to the initial position to lock onto its localization.

5.5.3 Postflight

The postflight operations included the delivery of ISS data files, imagery, and video from the experiments. Software as carefully configured to enable accurate, annotated, data recording for all desired test sessions. Downlink of this data was performed by NASA Ames, allowing reconstruction of the important on-orbit information detailing algorithm performance, discussed in the next section.

5.5.4 Anomalies

Due to the hardware anomalies that occurred on the Honey Astrobee in the hours before ReSWARM-1, ReSWARM-1 consisted of single-Astrobee operations with 28 tests. Afterwards, the Honey Astrobee was downmassed, and the Queen Astrobee was commissioned to bring back the multi-Astrobee capability on the

ISS. This delayed ReSWARM-2 by a few months, but with more time to finalize algorithms. A total of 39 successful test runs (an informal Astrobee test record) including multi-Astrobee tests which belonging to a separate investigation in ReSWARM-2 were later demonstrated.

6 Results: Microgravity Testing for On-Orbit Assembly

The three-step on-orbit assembly sample scenario, using the methods described in Section 4.6 was executed on the JEM on board the ISS. Results presented in the following sections are divided based on the key tools used for executing the on-orbit assembly sequence given in Fig. 5: The LQR_RRT* global planner for offline global planning in the presence of obstacles, the RATTLE information-aware motion planning framework with model improvement for learn-able parametric uncertainty, and tube MPC for robust tracking in the presence of disturbances. A section on planning and control speeds addresses real-time execution of these components on hardware, discussing computation times, time horizons, and other implementation details.

6.1 Experiment Set 1: LQR-RRT* Global Planning

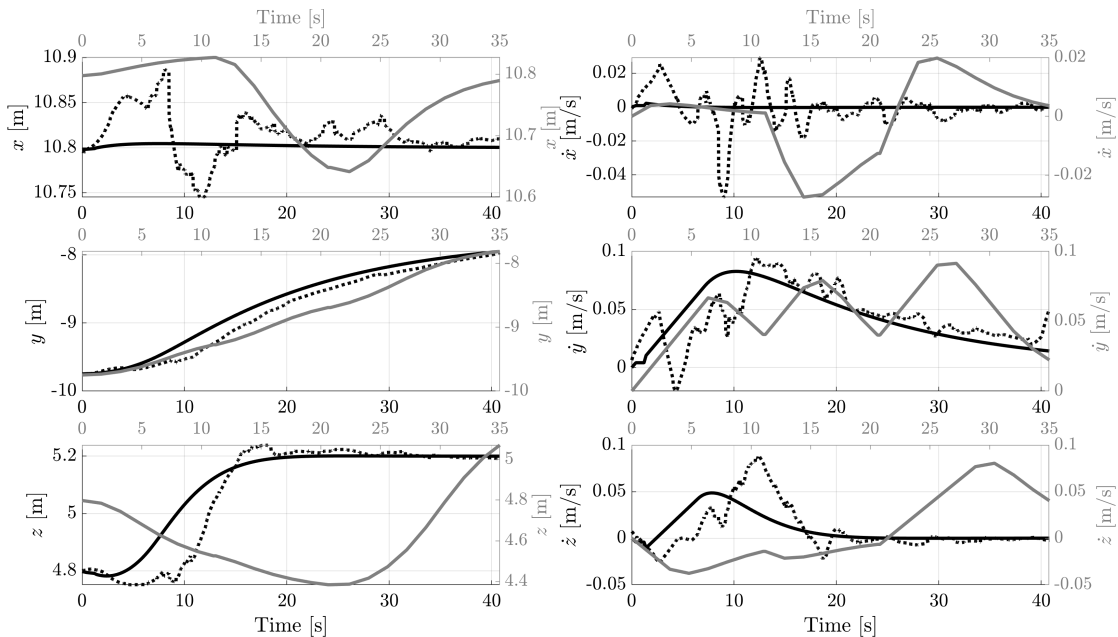


Figure 14: Translational trajectories for the Astrobee robot using LQR-RRT* (solid gray) and LQR shortcutting (solid black), and response from robust tube MPC (dotted black).

In this initial experiment, the Astrobee robot is tasked with moving between two points in the presence of obstacles. The obstacles present for this experiment include 6 safety ellipsoids which constrain the robot inside the test environment. Additionally, a static obstacle is generated inside the test environment. Trajectories are planned using LQR-RRT* and LQR shortcutting, and the planned trajectory is tracked using robust tube MPC to counteract disturbances. Figures 14 and 15 show the trajectories obtained from LQR-RRT* (solid gray line) and LQR shortcutting (solid black line), and the response from robust tube MPC (dotted black line). At specific points along the path, the LQR-RRT* trajectory is jerky and unnatural since the sampling stops once an initial trajectory which completes the path between Astrobee and the desired state is found. This trajectory is considered sub-optimal, but if the LQR-RRT* continued sampling the space through time, trajectories obtained would reach asymptotic optimality with respect to the cost function. For real-time hardware testing, computational efficiency is necessary for Astrobee to perform in real-world

conditions. Using the LQR-RRT* trajectory, an LQR shortcutted trajectory is found which takes a shorter amount of time to reach the desired target by taking shortcuts. The shortcutting method reduces the effects of randomness that occurs from sampling using LQR-RRT*. This final motion plan is then tracked using robust tube MPC which provides disturbance rejection control for the robot. For Fig. 15, note that the initial conditions for orientation of LQR-RRT* and LQR shortcutting differ from the initial condition of the controlled response of the Astrobee. This was an error in the algorithm which was resolved in further experiments, but the results obtained from the experiment still hold. In this case, the Astrobee would slew in response to the initial tracking error which would stabilize through time. Further discussion and comparisons to standard MPC is discussed in Subsection 6.3.

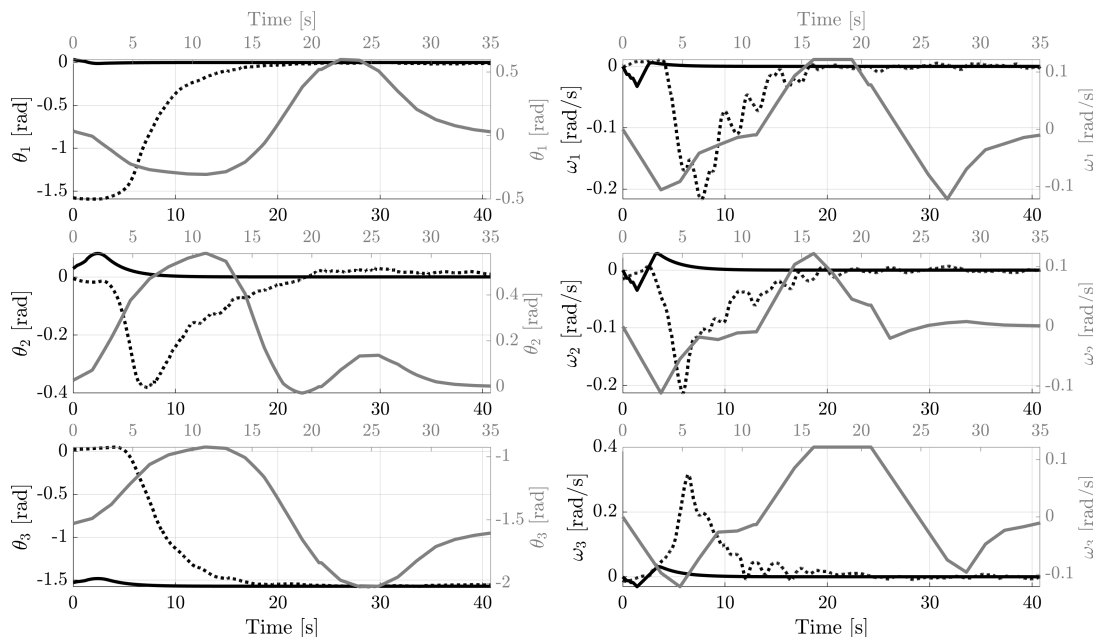


Figure 15: Attitude trajectories for the Astrobee robot using LQR-RRT* (solid gray) and LQR shortcutting (solid black), and response from robust tube MPC (dotted black).

6.2 Experiment Set 2: Information-Aware Planning and Model Estimation

Characteristic of system identification procedures (sysID) is a usually offline-planned purely excitation trajectory. Given a start and goal point, a criterion based on the nature and information content of the measured data is optimized in order to improve estimate accuracy. In contrast to sysID, RATTLE proposes an online trade-off between information-aware exciting motion and goal-directed motion. The online re-planning capabilities allow inclusion of latest model parameters as well as dynamic obstacles in the environment, resulting in more reactive and optimal plans. At the same time, RATTLE presents the ability to turn off exploratory motion once estimate covariance drops below a certain value, potentially conserving fuel and energy. The question then arises, whether an adjustable amount of information awareness can provide sufficient excitation for adequately estimating the parameters. The results presented in this section demonstrate the capabilities of RATTLE juxtaposed with that of a general sysID procedure, more specifically in what concerns ability to lend enough excitation for parameter convergence.

Fig. 16 illustrates the information content in both cases, i.e., a purely excitation trajectory, and an information-aware trajectory using RATTLE. In the latter case, the emphasis on information weighting is relaxed as the estimate covariance decreases, causing the information content to plateau. Note that the robot performed a final yaw maneuver to reach the goal point, resulting in greater information content for I_{zz} for the information-aware case. The excitation trajectory ran for 60 seconds and was executed during

an earlier micro-gravity test campaign, whereas the RATTLE results shown here were a part of the complete on-orbit assembly pipeline, with 40 seconds of RATTLE-based parameter learning during the 3 minute demonstration.

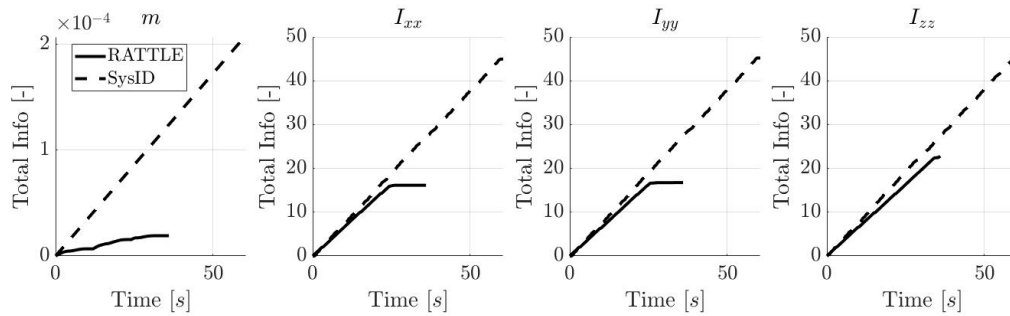


Figure 16: Information content, purely informative plan and RATTLE local plan. While both trajectories start off with similar trends of 'informativeness', particularly for the inertias, the information content of the RATTLE local plan shuts-off towards the end of the trajectory.

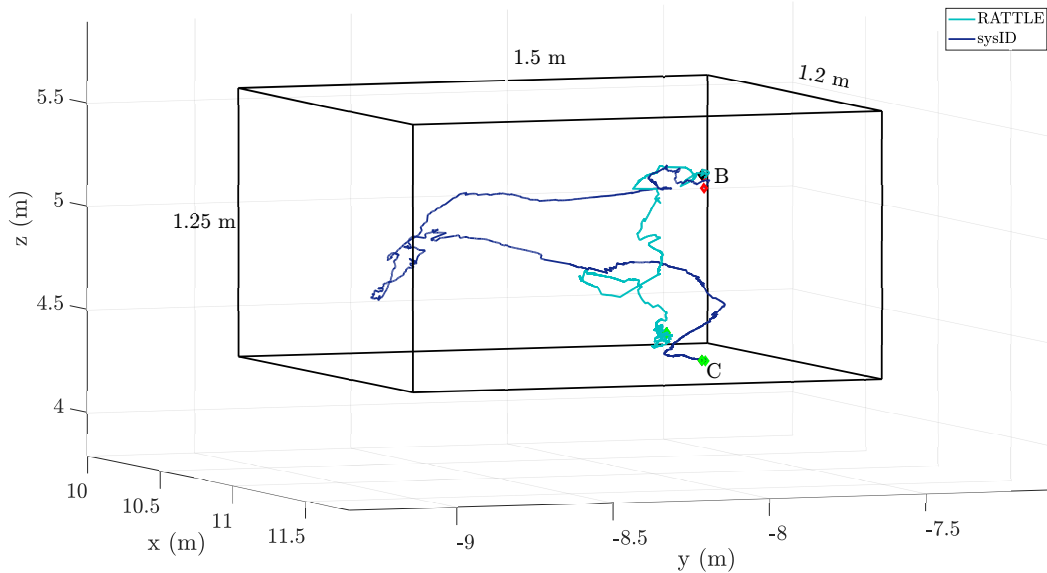


Figure 17: Trajectories executed in microgravity, sysID and RATTLE. Black lines denote the space constraints for the planners. The red and green diamond markers denote the points B and C in 3D space. The RATTLE plan seems to have skipped regulation at point C, regulating at the last node of the RRT global plan instead.

Tasks such as on-orbit assembly could benefit from the RATTLE algorithm's ability to replan, and reduce parametric uncertainty online. As illustrated in Fig. 5, assembly tasks could be cyclic in nature, with the robot collecting and transporting payload to its assembly location and precisely depositing it. In this context, parametric uncertainty and the resulting inability to predict robot behaviour could potentially compromise safe and precise execution of the assembly task. While robust control approaches could offer robustness guarantees against known bounded uncertainties, these approaches are often cautious and do not take into account recent system/uncertainty information. On the other hand, estimating uncertainty by performing full system identification for each assembly component could be redundant and non-economical in terms of fuel and time. To that end, RATTLE provides a reactive approach of online uncertainty reduction and incorporation of the latest system and environment information in subsequent optimal motion and robust

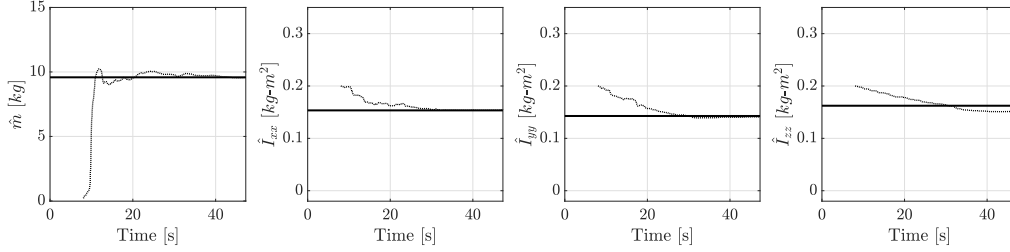


Figure 18: Inertial parameter estimates for the RATTLE case. Note that results shown here are obtained offline by replaying test data from the microgravity experiments.

control plans. Besides, as illustrated by the estimation plots in Fig. 18, sufficient information gain can be amassed on-the-fly without interrupting the primary task to perform full system ID. Additionally, the provision of online replanning is especially relevant in a single or multi-agent autonomous assembly scenario, where frequent online replanning might be needed as the assembled structure grows.

Parameter	% error	% cov. reduction
mass	0.39	99
I_{xx}	0.91	68
I_{yy}	1.35	49
I_{zz}	6.92	25

Table 3: Percent error of with respect to the true values of the inertial parameters and percent covariance reduction for the estimates shown in Fig.18

6.2.1 Improving estimation accuracy in the presence of noisy measurement data

Latency, localization outliers, and input saturation were some key elements that directly impacted the accuracy of inertia estimation. The issues of measurement data latency and input saturation, which were more pronounced on hardware, were identified at the time of simulation testing. On the other hand, the effect of localization outliers and scaling was discovered after the microgravity test sessions. This section briefly explains the effects and the algorithmic components put in place to deal with them.

- The parameter estimation algorithm received the robot states and commanded control inputs via the relevant ROS topics, denoted here as CTL for the control inputs, and EKF for the localization EKF data. The expected publication frequency of both these topics is 62.5 Hz. However, as Fig. 19 illustrates, latency occurred regularly on the resource-constrained hardware; the initial decrease in frequency is thought to arise from launching custom nodes and global plan computation. A time-stamp ordering algorithm was therefore implemented to synchronize data from the two sources before being passed on to the sequential estimator.
- As discussed in Section 5.1.3, the design of Astrobees FAM is such that the actual actuation could be quite different from the commanded values. Tight actuation constraints to prevent frequent force and torque saturation coupled with a custom module dubbed `inverse_fam` were put in place to deal with this issue. The `inverse_fam` module uses the nozzle opening angles (published by default via a dedicated ROS topic), and in a non-trivial inverse mixer process obtains the actually applied post-saturation forces and torques at each time step.
- Astrobees known mass estimates are regarded as "fairly accurate," therefore further investigation of the measurement data was carried out when the obtained estimates did not match the expected values. To troubleshoot the estimation algorithm further, the projected linear accelerations, i.e., those found by dividing the commanded forces by the known mass of Astrobees, were compared to

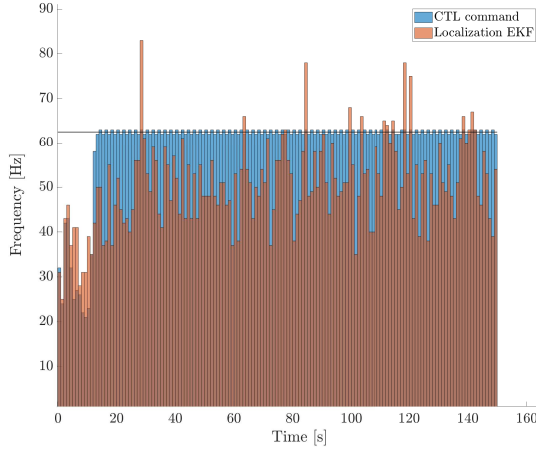


Figure 19: A histogram illustrating the frequency of the commanded control signals (CTL) and the localization estimates (EKF) on Astrobee hardware during a sample microgravity experiment. The bins correspond to the number of signals sent out per second (Hz). Note that the expected frequency of both signals is 62.5 Hz, as shown by the black line, but computation latency results in signals being dropped or delayed.

the measured accelerations, both quantities in body frame. A "scaling effect" was observed on the accelerations, with the measured accelerations being *higher* than the projected ones, considering the known estimate of Astrobee's mass as valid. This effect, observed in data recorded across all experiments, manifested differently for each axis. While the reason for these "stray accelerations" is still being investigated, the parameter estimator treats this as a known linear model in addition to Astrobee's dynamics. Linear least squares was used for calibration of the scaling parameters using micro-gravity data. The scaling factor per axis is denoted as s_i , where $i = \{x, y, z\}$. Measured linear accelerations recorded over all RATTLE on-orbit experiments were stacked per axis, resulting in vectors \mathbf{a}_i , where $i = \{x, y, z\}$. Similarly, the force vectors over multiple experiments are collected as \mathbf{f}_i . The known true mass of Astrobee is denoted as m , $m = 9.58kg$. Let $\theta = 1/m$ and $\theta' = 1/s$. This formulation of the scaling parameter makes it straightforward to incorporate this effect post-calibration in the sequential estimation framework of Section 4.4.1.

$$\theta_i^* = \operatorname{argmin} \|\mathbf{f}_i(\theta + \theta'_i) - \mathbf{a}_i\|_2^2 \quad (38)$$

$$\theta_i^* = (\mathbf{f}_i^T \mathbf{f}_i)^{-1} \mathbf{f}_i^T \mathbf{a}_i - \theta \quad (39)$$

- Owing to its minimization of the L_2 norm of the residuals, the least squares estimation is particularly sensitive to outliers, which can skew the fit. In the case of the ReSWARM micro-gravity experiments, sudden jumps in Astrobee's localization were a key reason for the loss of accuracy in the estimation procedure. Fig. 20 shows one such localization outlier as seen in the angular acceleration. Note that the angular accelerations were computed by numerical differentiation of the angular velocity data, resulting in amplification of the measurement noise. In the recursive least squares (or Kalman filter) formulation, Section 4.4.1, the innovation, or the difference between the observed and the predicted measurements based on the current estimate are given as

$$\gamma_k = \tilde{\mathbf{y}}_k - \mathbf{H}_k \hat{\boldsymbol{\theta}}_{k-1} \quad (40)$$

and the innovation covariance, $E[\gamma_k, \gamma_k^T]$, is

$$\mathbf{S}_k = \mathbf{H}_k \mathbf{P}_{k-1} \mathbf{H}_k^T + \mathbf{W} \quad (41)$$

If the assumption of randomly distributed Gaussian measurement noise from eq. (31) holds, then the normalized sum of innovations $\gamma_k \mathbf{S}_k^{-1} \gamma_k^T$, can be looked at as the Mahalanobis distance between

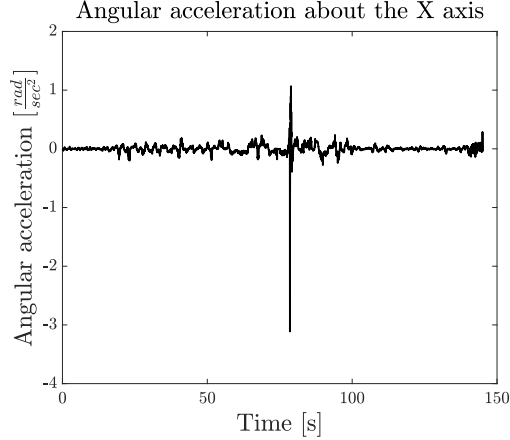


Figure 20: Angular acceleration showing localization outliers during a micro-gravity run. Apart from the jumps seen in the plot at 78 seconds, some other localization drifts can be seen. Fast motions that cause a loss of visual features, as well as external disturbance forces are thought to cause these effects.

the expected measurement based on the previous estimate and the actual measurement (Mirzaei and Roumeliotis, 2008). Based on the critical value of the χ_l^2 distribution at the desired confidence level, a probabilistic threshold can thus be set for $\gamma_k S_k^{-1} \gamma_k^T$ to determine measurement reliability. Here, l is the number of degrees of freedom, corresponding to the number of independently sampled normal distributions. In this case, l is equal to the number of measurements, $l = 6$ (linear and angular accelerations), as they are considered independent and identically distributed. The value corresponding to the probability level of 0.99 is chosen as the threshold ν , i.e., $P(\gamma_k S_k^{-1} \gamma_k^T \leq \nu) = 0.99$.

$$\gamma_k S_k^{-1} \gamma_k^T \in \chi_l^2 \quad (42)$$

For outlier rejection, if the result of the test was higher than a threshold $\gamma_k S_k^{-1} \gamma_k^T > \nu$, then the measurement was rejected and the update steps from eq. 4.4.1 were not performed.

6.3 Experiment Set 3: Robust Tracking

In addition to the on-orbit assembly scenario, a separate, dedicated set of experiments sought to demonstrate the performance benefits of robust tube MPC for trajectory tracking. Here, parametric uncertainty was ignored (the correct model was supplied). Astrobee was tasked with tracking a translational reference trajectory, with the only error sources present those inherent in Astrobee’s operation.⁵ The tracking task is shown in Fig. 21 (note that the image is reversed along the ISS y-axis).

The results of the tracking task are shown in Fig. 22. Robust tube MPC is more “sluggish” due to its tightened nominal constraints, but is generally better in counteracting disturbances due to its disturbance rejection controller. This is particularly obvious in Fig. 23, where inputs are plotted alongside position tracking performance. Here, the nominal (grey), disturbance rejection (white), and total (black) control inputs have been separately recorded from on-orbit data. Generally, the nominal MPC portion is relatively inactive if there are no major changes in trajectory tracking, particularly evident for the x-axis tracking which is unchanged for the duration of the trajectory. As seen in the z-axis tracking, nominal MPC activates to provide horizon guidance once upcoming trajectory changes come within view. Throughout, disturbance rejection control activates to counter disturbance sources. This experiment is a good example of robust tube MPC’s ability to provide a form of robustness in its tracking task. As shown later in Section 6.4, it is also feasible to run on resource-constrained hardware.

⁵While somewhat speculative, Astrobee’s chief disturbance contributor is its localization system, perhaps followed by the accuracy of its mixer. There are a variety of other error contributors, such as: an always-on cooling fan; air vents on the ISS; a rampdown/rampup period for Astrobee’s impeller system; and others.

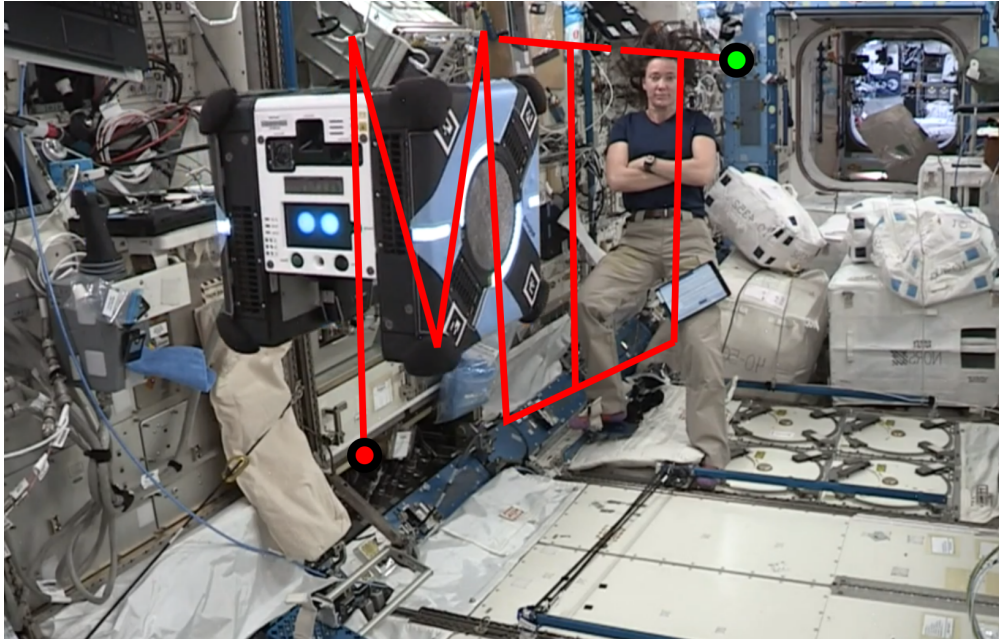


Figure 21: The tracking task's reference trajectory for robust tube MPC comparison.

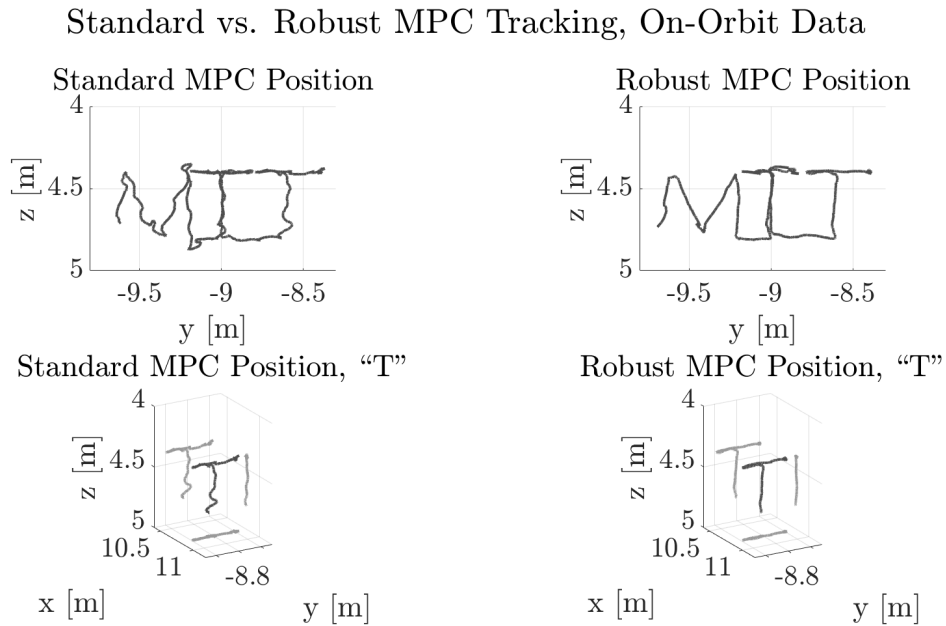


Figure 22: Tracking of the reference trajectory with standard MPC (left) and robust tube MPC (right), with the same cost function tuning values. A 3D view of the "T" portion of the trajectory is shown below. Note that a portion of the initial trajectory has been clipped during a transient period where Astrobee's impeller ramps down when swapping controllers.

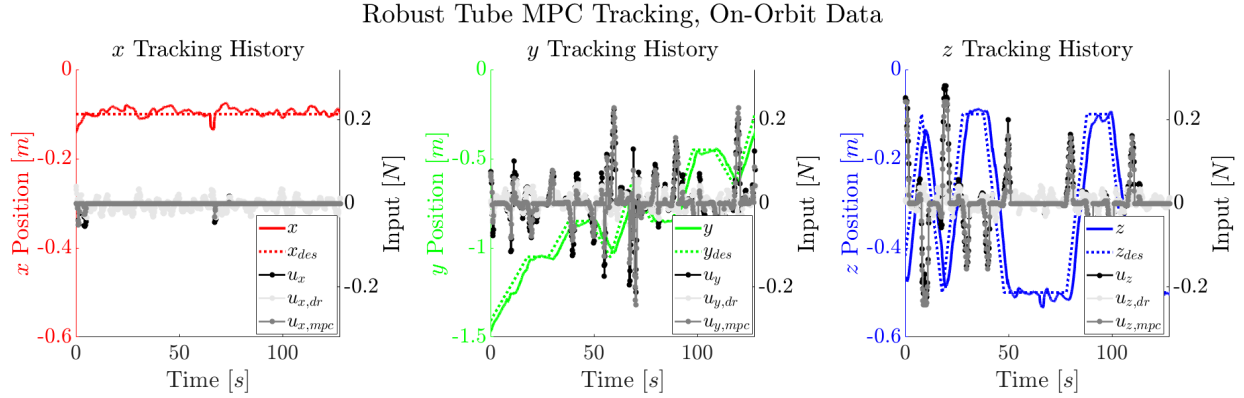


Figure 23: Translational tracking performance for the x-, y-, and z-axes, with robust tube MPC input components also shown. Robust tube MPC’s total input is the combination of a tightly-constrained nominal MPC and a disturbance rejection ancillary controller.

6.3.1 Robust tracking results for the On-Orbit Assembly Scenario

As mentioned in Subsection 4.6, the on-orbit assembly scenario involves 3 segments which the Astrobee moves from waypoint (a) to (b), (b) to (c), and (c) to (a) following the algorithmic elements found in Table 1. Additionally, a static obstacle is set between waypoints (a) to (b) and (c) to (a) to model the physical space where “construction components” reside.

For the first segment, the Astrobee moves from the construction site to the storage area to “manipulate” a component for construction. At this part of the scenario, the system model knowledge is adequate with no inertial uncertainty, so standard MPC is used. The Astrobee obtains collision-free trajectories (using LQR-RRT* and LQR shortcutting) and tracks the motion plan which is shown in Fig. 24.

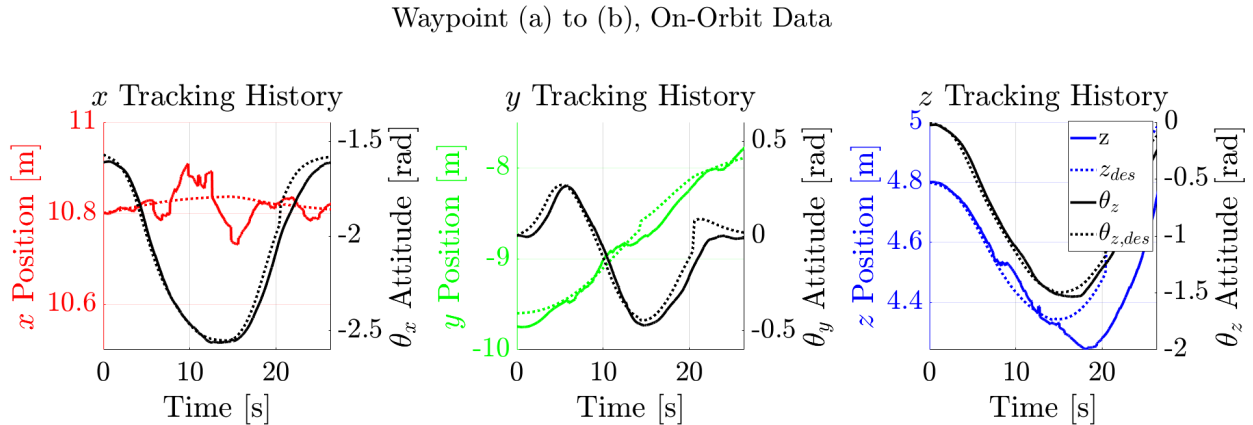


Figure 24: Translational and attitude histories of the Astrobee tracking a LQR-RRT* plan en route from (a) to (b).

Waypoint (b) to (c), On-Orbit Data

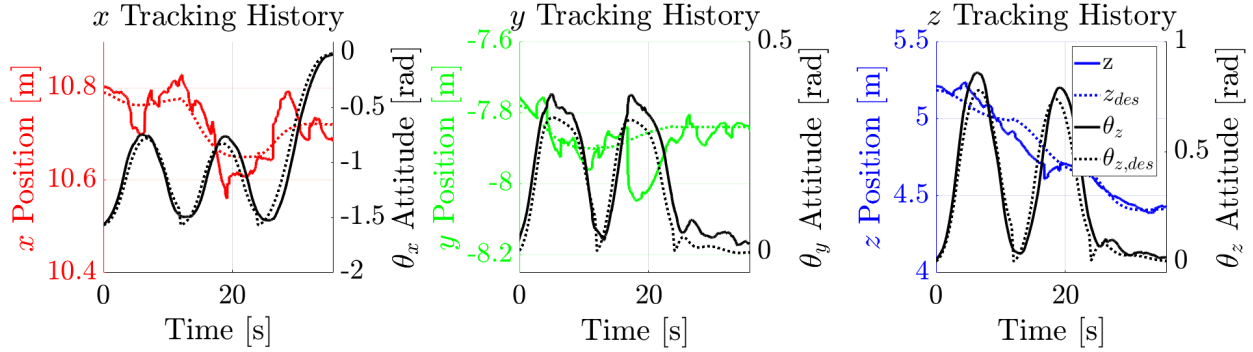


Figure 25: Translational and attitude histories of the Astrobee tracking an information rich plan en route from (b) to (c).

The second segment involves the Astrobee moving from storage area (b) to a safe area (c). During this segment, it is assumed that the Astrobee has already manipulated the object, thus the system model knowledge of the inertial parameters are poor. The RATTLE algorithm is used to plan and estimate the inertial parameters while updating the system model to better the controlled response. Fig. 25 shows the information rich trajectory and the robust tube MPC controlled response using the RATTLE algorithm. Fig. 17 shows the real-time planning of the RATTLE motion planner which is used in conjunction with the robust tube MPC controller and sequential least squares to update the system model. Once Astrobee reaches waypoint (c), Astrobee has a sufficient model of the learned inertial parameters to move onto the next segment.

With the inertial parameters learned, the Astrobee system model is sufficient, and the Astrobee moves from the safe area (c) back to the construction site (a). A high-level collision-free motion plan is formed using LQR-RRT* and LQR shortcutting to avoid the obstacle between the two waypoints. With the learned system model, uncertainty is still present, thus robust tube MPC is used to mitigate this disturbance as it tracks the motion plan. Fig. 26 shows the motion plan and the robust tube MPC response for this segment.

The localization error played a significant role in the tracking accuracy of the Astrobee system. This is much more apparent in the (c) to (a) segment. At position (a), the Astrobee is much closer to features allowing for more accurate localization estimates, but the position at (c) is further from these features which increases the variability in localization error. Comparing Fig. 26 to 24, the tracking error in all three directions is much more significant in the (c) to (a) segment. The “jumps” in the tracking error from Astrobee’s rotational motion is due to this localization error. The increase in localization error is due to the decrease in feature count which is attributed to distance from the features, physical changes to the experimental module that can hide features, and rotational velocity of the Astrobee when collecting features. These contributions to the localization error were mitigated as much as possible during the experiment, yet the localization error produced a significant effect on the tracking response for the experiment.

Waypoint (c) to (a), On-Orbit Data

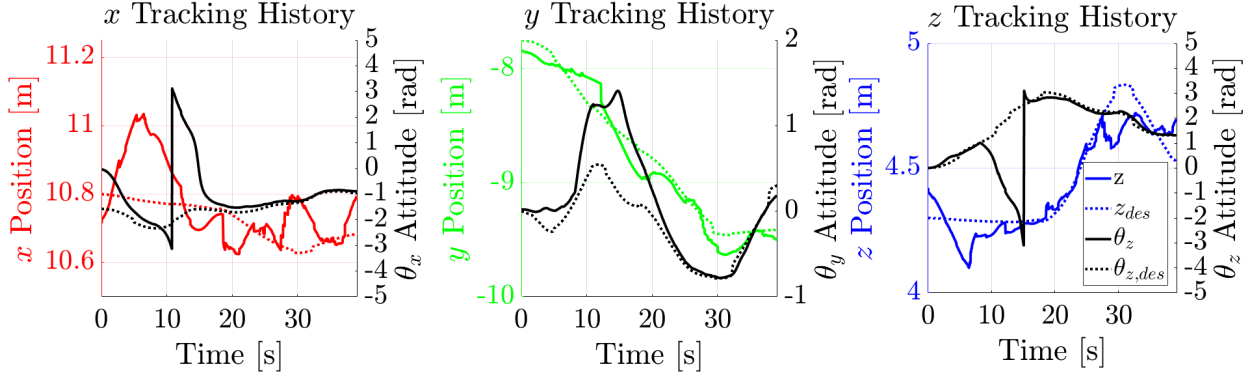


Figure 26: Translational and attitude histories of the Astrobee tracking a LQR-RRT* plan en route from (c) to (a).

Table 4: Replan periods and approximate actual computational time taken for computation on Astrobee’s Snapdragon processors on-orbit.

Component	Replan Period [s]	Hardware Speed [s]
Global Planner (LQR-RRT*)	as-needed	0.5 – 2
Global Planner (kino-RRT)	as-needed	0.5 – 2
Local Planner (RATTLE only)	12	2 – 7
Controller	0.2	0.05 – 0.2

6.4 Planning and Control Speeds on resource-constrained hardware

Finally, online planning and control computational speeds are considered aboard Astrobee, an important consideration when discussing real-time use on hardware. Planning/control periods and approximate hardware-demonstrated values are shown in Fig. 4. For example, the computational speed of an example run using the robust tube MPC is shown in Fig. 27. While outlier periods do exceed the desired computational period, average computational time is within the desired 0.2 [s] computational period (0.1604 ± 0.0503 [s]). Exact processor details are provided in (Smith et al., 2016b); significant effort went into ensuring components met their expected rates. Planning and control periods had to be carefully chosen in a tradeoff between increasing optimality for longer horizons, the frequency of incorporating desired updates for replanning (especially for the local planner), and the computational realities of the Astrobee processors. A notable difference on-orbit compared to ground testing was the increased load for the default localization system, which has to contend with a larger map and a greater number of features, and other flight software components, resulting in an approximately $\times 2$ slowdown compared to ground tests.

Simulation-Based Benchmark Data for Optimization-Based Solvers RATTLE’s local planner and the robust tube MPC controller ultimately rely on optimization solvers to handle online computation of reference trajectories and control inputs, respectively (see Section 4). Simulation benchmark details of these components are provided for a better understanding of their performance and their comparison to similar

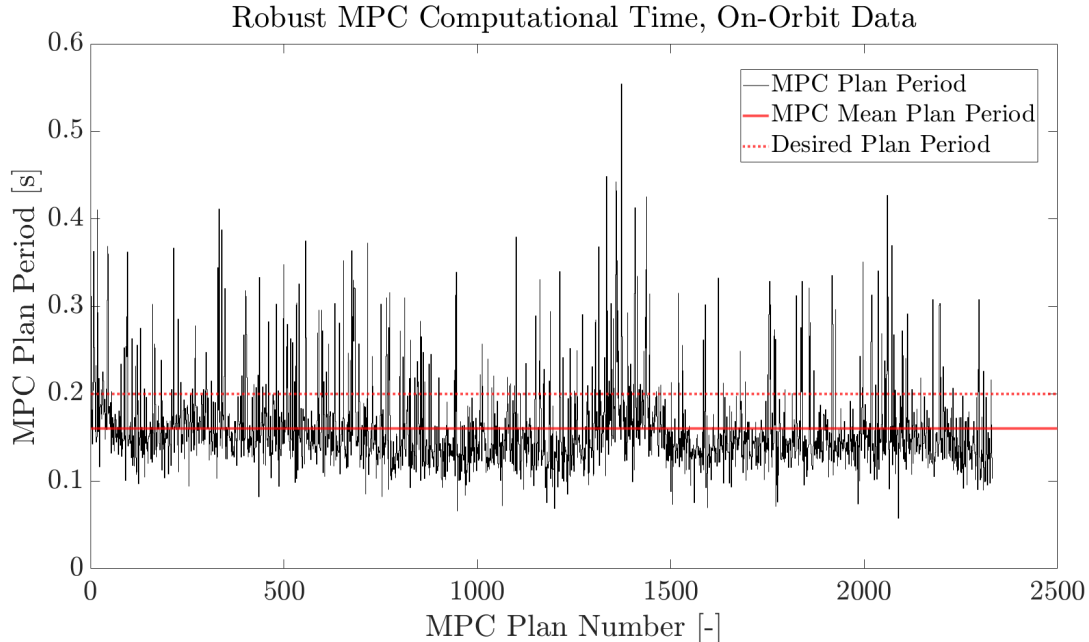


Figure 27: Typical planning periods for robust tube MPC onboard the Astrobee free-flyer, shown here for a multi-waypoint maneuvering task.

optimization-based solutions.

The information-aware local planner uses ACADO (Houska et al., 2011), a software toolkit for solving optimal control problems. ACADO relies on a direct multiple shooting discretization with an SQP solution method, with QPOASES as the default QP solver (Ferreau et al., 2014). Well-suited for optimal control problems, ACADO uses a real-time iteration (RTI) scheme, whereby the quadratic approximation to the true NLP is constructed in separate preparation and computation phases for each SQP iteration, allowing problem preparation to occur before measurements are received. Multiple iterations may be performed if greater local convergence accuracy is desired—this is the approach taken by RATTLE, performing as many iterations as possible until convergence criteria fall below a designated threshold or computation time runs short. The KKT conditions are used as an approximation of convergence quality. Meanwhile, the robust tube model predictive controller also uses QPOASES, with CasADi as the front-end for specifying the optimal control problem (Andersson et al., 2019). The robust tube MPC benchmark uses on-orbit data from a sample reference trajectory, with simulated disturbance error sampled from a uniform distribution. Ultimately, both solution methods rely on the online solution of quadratic programs—in the case of the local planner, as the backend to a nonlinear programming solution method.

Table 5 compares some benchmarking data for each of these solvers for simulation data of plans with horizons equivalent to that used in later hardware demonstrations ($N = 40$ for local planning, $N = 5$ for robust control). KKT tolerance is used as a convergence benchmark for SQP. 5 SQP iterations are performed for the local planner, near the maximum permissible iterations on hardware while reliably remaining within a replanning period of 12 [s]. The local planner benchmark includes information weighting on moments of inertia and mass for an approximately 0.5 [m] offset waypoint planning task using the 6DOF Newton-Euler dynamics. The tube MPC, meanwhile, is solved exactly at each call using QPOASES for a sinusoidal tracking task for the double integrator dynamics. Benchmark data uses the same typical “laptop” hardware used for global planning shown above. Note that planning/control periods and rates are explicitly crafted to be sufficient for use on Astrobee’s more limited processors, detailed in Section 6.4.

⁶Note that ACADO uses a direct multiple shooting approach, where the full state need only be provided at a number of “shooting nodes.” This 40-timestep solution uses only 6 input variables, hence 240 QP decision variables.

Table 5: Computation timing on representative benchmark problems for the local planner and controller in simulation.

Module	Problem Size [dec. vars.]	Problem Class	Solver(s)	Benchmark Solve Time [s]	Convergence Data
Local Planner (N=40)	240 ⁶	NLP	ACADO RTI SQP solver, QPOASES	0.929	4.53×10^{-4} (KKT stationarity norm)
Controller (N=5)	51	QP	QPOASES (and qrpq)	0.00849	0.0 (exact convergence)

7 Conclusion and Discussion

Robotic spacecraft executing on-orbit operations must address autonomy challenges such as collision-avoiding motion planning in dynamic environments and ensuring control accuracy in the presence of changing system models. To that end, this work develops planning, control, and model learning frameworks for tackling these challenges, and presents micro-gravity experimentation results from the ReSWARM flight experiments on NASA’s Astrobee free-flyer on the International Space Station. Considering an on-orbit assembly scenario, RELative Satellite sWarming and Robotic Maneuvering, or ReSWARM, demonstrated the following key technologies: (1) Sampling-based global planning taking into account system dynamics, (2) information-aware planning and model learning for on-orbit reconfiguration, and (3) robust tracking in the presence of model uncertainty. Further, extensive hardware implementation details and challenges that future autonomous free-flyers will need to considered are presented.

The demonstrated framework for microgravity testing provides the capabilities for safe, modular, close proximity operation. These strategies are repurposable to other on-orbit autonomy tasks that require efficiency from a safety standpoint. By demonstrating these technologies on practical hardware tests, the framework can feasibly be incorporated in new emerging space robotic systems for larger and more complex on-orbit close proximity applications. Future work will entail physical manipulation of objects to further validate the on-orbit assembly demonstration, consideration of physical objects for real-time mapping and collision avoidance, and bringing the information-theoretic framework to a greater set of uncertain robots.

Acknowledgments

This research was supported by an appointment to the Intelligence Community Postdoctoral Research Fellowship Program at Massachusetts Institute of Technology, administered by Oak Ridge Institute for Science 16 and Education through an interagency agreement between the U.S. Department of Energy and the Office of the Director of National Intelligence. Funding for this work was also provided by the NASA Space Technology Mission Directorate through a NASA Space Technology Research Fellowship under grant 80NSSC17K0077. This work was also supported by the Portuguese Science Foundation (FCT) grant PD/BD/150632/2020, the LARSyS - FCT Plurianual funding 2020-2023, and an MIT Seed Project under the MIT Portugal Program. International Space Station (ISS) experiments were conducted under ISS National Lab user agreement UA-2019-969 as part of the Relative Satellite sWarming and Robotic Maneuvering (ReSWARM) investigations. The researchers would especially like to thank Brian Coltin, Marina Moreira, Ruben Garcia Ruiz, Ryan Soussan, Jose Benavides, Jose Cortez, Aric Katterhagen, and the rest of the Astrobee operations team at NASA Ames. The authors gratefully acknowledge the support that enabled this research.

References

- Albee, K. (2019). *Toward Optimal Motion Planning for Dynamic Robots: Applications On-Orbit*. Thesis, Massachusetts Institute of Technology.
- Albee, K., Ekal, M., Coltin, B., Ventura, R., Linares, R., and Miller, D. W. (2022). The rattle motion planning algorithm for robust online parametric model improvement with on-orbit validation. *arXiv preprint arXiv:2203.01547*.

- Albee, K., Ekal, M., and Oestreich, C. (2020). A brief guide to Astrobotic’s flight software.
- Albee, K., Ekal, M., Ventura, R., and Linares, R. (2019). Combining parameter identification and trajectory optimization: Real-time planning for information gain. *arXiv preprint arXiv:1906.02758*.
- Albee, K. E. S. (2022). *Online Information-Aware Motion Planning with Model Improvement for Uncertain Mobile Robotics*. PhD thesis, Massachusetts Institute of Technology.
- Andersson, J. A., Gillis, J., Horn, G., Rawlings, J. B., and Diehl, M. (2019). CasADi: A software framework for nonlinear optimization and optimal control. *Mathematical Programming Computation*, 11(1):1–36.
- Armstrong, B. (1989). On finding exciting trajectories for identification experiments involving systems with nonlinear dynamics. *The International journal of robotics research*, 8(6):28–48.
- Badawy, A. and McInnes, C. R. (2008). On-orbit assembly using superquadric potential fields. *Journal of Guidance, Control, and Dynamics*, 31(1):30–43.
- Bellman, R. et al. (1954). The theory of dynamic programming. *Bulletin of the American Mathematical Society*, 60(6):503–515.
- Bonalli, R., Cauligi, A., Bylard, A., and Pavone, M. (2019). GuSTO: Guaranteed sequential trajectory optimization via sequential convex programming. In *International Conference on Robotics and Automation (ICRA)*. IEEE.
- Brunke, L., Greeff, M., Hall, A. W., Yuan, Z., Zhou, S., Panerati, J., and Schoellig, A. P. (2021). Safe learning in robotics: From learning-based control to safe reinforcement learning. *Annual Review of Control, Robotics, and Autonomous Systems*.
- Bualat, M., Barlow, J., Fong, T., Provencher, C., and Smith, T. (2015). Astrobotic: Developing a free-flying robot for the international space station. In *AIAA SPACE 2015 Conference and Exposition*, page 4643.
- Buckner, C. and Lampariello, R. (2018). *Tube-Based Model Predictive Control for the Approach Maneuver of a Spacecraft to a Free-Tumbling Target Satellite*. PhD thesis.
- Coll, G. T., Webster, G., Pankiewicz, O., Schlee, K., Aranyos, T., Nufer, B., Fothergill, J., Tamasy, G., Kandula, M., Felt, A., et al. (2020). Satellite servicing projects division restore-1 propellant transfer subsystem progress 2020. In *AIAA Propulsion and Energy 2020 Forum*, page 3795.
- Coumans, E. Bullet 2.83 Physics SDK Manual. page 40.
- Crassidis, J. L. and Junkins, J. L. (2004). *Optimal estimation of dynamic systems*. Chapman and Hall/CRC.
- Doerr, B., Albee, K., Ekal, M., Linares, R., and Ventura, R. (2021). Safe and uncertainty-aware robotic motion planning techniques for agile on-orbit assembly. In *2021 Space Flight Mechanics Meeting*.
- Doerr, B. and Linares, R. (2020). Motion planning and control for on-orbit assembly using lqr-rrt* and nonlinear mpc. *arXiv preprint arXiv:2008.02846*.
- Dogar, M., Knepper, R. A., Spielberg, A., Choi, C., Christensen, H. I., and Rus, D. (2015). Multi-scale assembly with robot teams. *The International Journal of Robotics Research*, 34(13):1645–1659.
- Dubowsky, S. and Papadopoulos, E. (1993). The Kinematics, Dynamics, and Control of Free-Flying and Free-Floating Space Robotic Systems. *IEEE Transactions on Robotics and Automation*.
- Ekal, M., Albee, K., Coltin, B., Ventura, R., Linares, R., and Miller, D. W. (2021). Online information-aware motion planning with inertial parameter learning for robotic free-flyers. In *2021 IEEE/RSJ International Conference on Intelligent Robots and Systems (IROS)*, pages 8766–8773. IEEE.
- Espinoza, A. T. and Roascio, D. (2017). Concurrent adaptive control and parameter estimation through composite adaptation using model reference adaptive control/Kalman Filter methods. *1st Annual IEEE Conference on Control Technology and Applications, CCTA 2017*, 2017-January:662–667.

- Ferreau, H. J., Kirches, C., Potschka, A., Bock, H. G., and Diehl, M. (2014). qpOASES: A parametric active-set algorithm for quadratic programming. *Mathematical Programming Computation*, 6(4):327–363.
- Flückiger, L., Browne, K., Coltin, B., Fusco, J., Morse, T., and Symington, A. (2018). Astrobotic Robot Software: Enabling Mobile Autonomy on the ISS. Technical report.
- Geraerts, R. and Overmars, M. H. (2007). Creating high-quality paths for motion planning. *The international journal of robotics research*, 26(8):845–863.
- Goward, S. N., Masek, J. G., Williams, D. L., Irons, J. R., and Thompson, R. (2001). The landsat 7 mission: Terrestrial research and applications for the 21st century. *Remote Sensing of Environment*, 78(1-2):3–12.
- Gralla, E. L. and De Weck, O. L. (2007). Strategies for on-orbit assembly of modular spacecraft. *Journal of the British Interplanetary Society*, 60(6):219–227.
- Hauser, K. and Ng-Thow-Hing, V. (2010). Fast smoothing of manipulator trajectories using optimal bounded-acceleration shortcuts. In *2010 IEEE international conference on robotics and automation*, pages 2493–2498. IEEE.
- Houska, B., Ferreau, H. J., and Diehl, M. (2011). ACADO toolkit—An open-source framework for automatic control and dynamic optimization: ACADO TOOLKIT. *Optimal Control Applications and Methods*, 32(3):298–312.
- Hoyt, R. P. (2013). Spiderfab: An architecture for self-fabricating space systems. In *AIAA Space 2013 conference and exposition*, page 5509.
- Inaba, M. and Corke, P., editors (2016). *Robotics Research*. Springer International Publishing.
- Izzo, D., Pettazzi, L., and Ayre, M. (2005). Mission concept for autonomous on-orbit assembly o... In *56th International Astronautical Congress of the International Astronautical Federation, the International Academy of Astronautics, and the International Institute of Space Law*, pages D1–4.
- Jenett, B., Abdel-Rahman, A., Cheung, K., and Gershenfeld, N. (2019). Material-robot system for assembly of discrete cellular structures. *IEEE Robotics and Automation Letters*, 4(4):4019–4026.
- Jewison, C., Erwin, R. S., and Saenz-Otero, A. (2015). Model Predictive Control with ellipsoid obstacle constraints for spacecraft rendezvous. *IFAC-PapersOnLine*, 28(9):257–262.
- Jewison, C., Sternberg, D., McCarthy, B., Miller, D. W., and Saenz-Otero, A. (2014). Definition and testing of an architectural tradespace for on-orbit assemblers and servicers.
- Jewison, C. M. (2014). *Reconfigurable Thruster Selection Algorithms for Aggregative Spacecraft Systems*. PhD thesis.
- Jewison, C. M. (2017). *Guidance and control for multi-stage rendezvous and docking operations in the presence of uncertainty*. PhD thesis, Massachusetts Institute of Technology.
- Kalakrishnan, M., Chitta, S., Theodorou, E., Pastor, P., and Schaal, S. (2011). Stomp: Stochastic trajectory optimization for motion planning. In *2011 IEEE international conference on robotics and automation*, pages 4569–4574. IEEE.
- Kallmann, M., Aubel, A., Abaci, T., and Thalmann, D. (2008). Planning collision-free reaching motions for interactive object manipulation and grasping. In *ACM SIGGRAPH 2008 classes*, pages 1–11.
- Karaman, S. and Frazzoli, E. (2011). Sampling-based algorithms for optimal motion planning. *The international journal of robotics research*, 30(7):846–894.
- Keim, J. A., Acikmese, A. B., and Shields, J. F. (2006). Spacecraft inertia estimation via constrained least squares. In *2006 IEEE Aerospace Conference*, pages 6–pp. IEEE.

- LaValle, S. M. (2001). RRT-progress and prospects. In *Algorithmic and Computational Robotics: New Directions*.
- Lee, G., Srinivasa, S. S., and Mason, M. T. (2017). Gp-ilqg: Data-driven robust optimal control for uncertain nonlinear dynamical systems. *arXiv preprint arXiv:1705.05344*.
- Lichter, M. D. and Dubowsky, S. (2004). State, shape, and parameter estimation of space objects from range images. In *IEEE International Conference on Robotics and Automation, 2004. Proceedings. ICRA'04. 2004*, volume 3, pages 2974–2979. IEEE.
- Limon, D., Alvarado, I., Alamo, T., and Camacho, E. (2008). On the design of robust tube-based MPC for tracking. *IFAC Proceedings Volumes (IFAC-PapersOnline)*, 17(1 PART 1):15333–15338.
- Lopez, B. T. (2019). *Adaptive robust model predictive control for nonlinear systems*. PhD thesis, Massachusetts Institute of Technology.
- Lopez, B. T., Howl, J. P., and Slotine, J.-J. E. (2019). Dynamic tube mpc for nonlinear systems. In *2019 American Control Conference (ACC)*, pages 1655–1662. IEEE.
- Lopez, B. T., Slotine, J.-J. E., and How, J. P. (2020). Adaptive Safety for Uncertain Nonlinear Systems with Control Barrier Functions and Contraction Metrics.
- Ma, O., Dang, H., and Pham, K. (2008). On-orbit identification of inertia properties of spacecraft using a robotic arm. *Journal of guidance, control, and dynamics*, 31(6):1761–1771.
- Majumdar, A. and Tedrake, R. (2017). Funnel libraries for real-time robust feedback motion planning. *International Journal of Robotics Research*, 36(8):947–982.
- Markley, F. L. and Crassidis, J. L. (2014). *Fundamentals of spacecraft attitude determination and control*, volume 33. Springer.
- Mayne, D. Q., Kerrigan, E. C., and Falugi, P. (2011). Robust model predictive control: Advantages and disadvantages of tube-based methods. *IFAC Proceedings Volumes (IFAC-PapersOnline)*, 44(1 PART 1):191–196.
- Mayne, D. Q., Seron, M. M., and Raković, S. (2005). Robust model predictive control of constrained linear systems with bounded disturbances. *Automatica*, 41(2):219–224.
- McInnes, C. R. (1995). Distributed control of maneuvering vehicles for on-orbit assembly. *Journal of Guidance, Control, and Dynamics*, 18(5):1204–1206.
- McQuade, F. and McInnes, C. R. (1997). Autonomous control for on-orbit assembly using potential function methods. *The Aeronautical Journal*, 101(1006):255–262.
- Miller, D., Saenz-Otero, A., Wertz, J., Chen, A., Berkowski, G., Brodel, C., Carlson, S., Carpenter, D., Chen, S., Cheng, S., Feller, D., Jackson, S., Pitts, B., Perez, F., and Szuminski, J. (2000). Spheres: A testbed for long duration satellite formation flying in micro-gravity conditions. *Advances in the Astronautical Sciences*, 105 I:167–179.
- Mirzaei, F. M. and Roumeliotis, S. I. (2008). A kalman filter-based algorithm for imu-camera calibration: Observability analysis and performance evaluation. *IEEE transactions on robotics*, 24(5):1143–1156.
- Okamoto, K. and Tsiotras, P. (2019). Optimal Stochastic Vehicle Path Planning Using Covariance Steering. *IEEE Robotics and Automation Letters*, 4(3):2276–2281.
- Ostafew, C. J., Schoellig, A. P., Barfoot, T. D., and Collier, J. (2016). Learning-based nonlinear model predictive control to improve vision-based mobile robot path tracking. *Journal of Field Robotics*, 33(1):133–152.
- Paden, B., Čáp, M., Yong, S. Z., Yershov, D., and Frazzoli, E. (2016). A survey of motion planning and control techniques for self-driving urban vehicles. *IEEE Transactions on intelligent vehicles*, 1(1):33–55.

- Patane, S., Joyce, E. R., Snyder, M. P., and Shestople, P. (2017). Archinaut: In-space manufacturing and assembly for next-generation space habitats. In *AIAA SPACE and astronautics forum and exposition*, page 5227.
- Perez, A., Platt, R., Konidaris, G., Kaelbling, L., and Lozano-Perez, T. (2012). Lqr-rrt*: Optimal sampling-based motion planning with automatically derived extension heuristics. In *2012 IEEE International Conference on Robotics and Automation*, pages 2537–2542. IEEE.
- Petersen, K. H., Nagpal, R., and Werfel, J. K. (2011). Termes: An autonomous robotic system for three-dimensional collective construction. *Robotics: science and systems VII*.
- Rackl, W., Lampariello, R., and Albu-Schäffer, A. (2013). Parameter identification methods for free-floating space robots with direct torque sensing. *IFAC Proceedings Volumes*, 46(19):464–469.
- Raković, S. V. and Levine, W. S. (2019). *Handbook of Model Predictive Control*. Springer.
- Ratliff, N., Zucker, M., Bagnell, J. A., and Srinivasa, S. (2009). Chomp: Gradient optimization techniques for efficient motion planning. In *2009 IEEE International Conference on Robotics and Automation*, pages 489–494. IEEE.
- Reed, B. B., Smith, R. C., Naasz, B. J., Pellegrino, J. F., and Bacon, C. E. (2016). The restore-1 servicing mission. In *AIAA space 2016*, page 5478.
- Saleh, J. H., Lamassoure, E. S., Hastings, D. E., and Newman, D. J. (2003). Flexibility and the value of on-orbit servicing: New customer-centric perspective. *Journal of Spacecraft and Rockets*, 40(2):279–291.
- Sathya, A., Sotasakis, P., Van Parys, R., Themelis, A., Pipeleers, G., and Patrinos, P. (2018). Embedded nonlinear model predictive control for obstacle avoidance using panoc. In *2018 European control conference (ECC)*, pages 1523–1528. IEEE.
- Schulman, J., Ho, J., Lee, A. X., Awwal, I., Bradlow, H., and Abbeel, P. (2013). Finding locally optimal, collision-free trajectories with sequential convex optimization. In *Robotics: science and systems*, volume 9, pages 1–10. Citeseer.
- Settles, B. (2009). Active learning literature survey. Computer Sciences Technical Report 1648, University of Wisconsin–Madison.
- Shi, L., Kinkaid, N., and Katupitiya, J. (2016). Robust control for satellite attitude regulation during on-orbit assembly. *IEEE Transactions on Aerospace and Electronic Systems*, 52(1):49–59.
- Siciliano, B. and Khatib, O. (2016). *Springer handbook of robotics*. Springer.
- Singh, S., Majumdar, A., Slotine, J. J., and Pavone, M. (2017). Robust online motion planning via contraction theory and convex optimization. In *IEEE International Conference on Robotics and Automation*, pages 5883–5890. IEEE.
- Slade, P., Culbertson, P., Sunberg, Z., and Kochenderfer, M. (2017). Simultaneous active parameter estimation and control using sampling-based bayesian reinforcement learning. In *2017 IEEE/RSJ International Conference on Intelligent Robots and Systems (IROS)*, pages 804–810. IEEE.
- Smith, T., Barlow, J., Bualat, M., Fong, T., Provencher, C., Sanchez, H., and Smith, E. (2016a). Astrobee: A new platform for free-flying robotics on the international space station. In *International Symposium on Artificial Intelligence, Robotics, and Automation in Space (iSAIRAS)*, number ARC-E-DAA-TN31584.
- Smith, T., Barlow, J., Bualat, M., Fong, T., Provencher, C., Sanchez, H., and Smith, E. (2016b). Astrobee: A New Platform for Free-Flying Robotics on the ISS. In *iSAIRAS 2016*.
- Soussan, R., Kumar, V., Coltin, B., and Smith, T. (2022). Astroloc: An efficient and robust localizer for a free-flying robot. In *2022 International Conference on Robotics and Automation (ICRA)*, pages 4106–4112. IEEE.

- Stella, L., Themelis, A., Sopasakis, P., and Patrinos, P. (2017). A simple and efficient algorithm for nonlinear model predictive control. In *2017 IEEE 56th Annual Conference on Decision and Control (CDC)*, pages 1939–1944. IEEE.
- Van Loan, C. (1978). Computing integrals involving the matrix exponential. *IEEE transactions on automatic control*, 23(3):395–404.
- VanDyke, M. C., Schwartz, J. L., Hall, C. D., et al. (2004). Unscented kalman filtering for spacecraft attitude state and parameter estimation. *Advances in the Astronautical Sciences*, 118(1):217–228.
- Webb, D. J., Crandall, K. L., and van den Berg, J. (2014). Online parameter estimation via real-time replanning of continuous gaussian pomdps. In *2014 IEEE International Conference on Robotics and Automation (ICRA)*, pages 5998–6005. IEEE.
- Wensing, P. M., Kim, S., and Slotine, J.-J. E. (2017). Linear matrix inequalities for physically consistent inertial parameter identification: A statistical perspective on the mass distribution. *IEEE Robotics and Automation Letters*, 3(1):60–67.
- Werfel, J., Petersen, K., and Nagpal, R. (2014). Designing collective behavior in a termite-inspired robot construction team. *Science*, 343(6172):754–758.
- Willmann, J., Augugliaro, F., Cadalbert, T., D’Andrea, R., Gramazio, F., and Kohler, M. (2012). Aerial robotic construction towards a new field of architectural research. *International journal of architectural computing*, 10(3):439–459.
- Wilson, A. D. and Murphey, T. D. (2015). Maximizing fisher information using discrete mechanics and projection-based trajectory optimization. In *2015 IEEE International Conference on Robotics and Automation (ICRA)*, pages 2403–2409. IEEE.
- Wilsona, E., Suttera, D. W., and Mahb, R. W. (2004). Mcrls for on-line spacecraft mass-and thruster-property identification. In *Proceedings of the IASTED international conference on intelligent systems and control*.
- Wu, Y.-H., Yu, Z.-C., Li, C.-Y., He, M.-J., Hua, B., and Chen, Z.-M. (2020). Reinforcement learning in dual-arm trajectory planning for a free-floating space robot. *Aerospace Science and Technology*, 98:105657.
- Yi-King Choi, Jung-Woo Chang, Wenping Wang, Myung-Soo Kim, and Elber, G. (2009). Continuous Collision Detection for Ellipsoids. *IEEE Transactions on Visualization and Computer Graphics*, 15(2):311–325.
- Yoshida, K. and Abiko, S. (2002). Inertia parameter identification for a free-flying space robot. In *AIAA Guidance, Navigation, and Control Conference and Exhibit*, page 4568.